

# Isotope Shift Measurements of Stable and Short-Lived Lithium Isotopes for Nuclear Charge Radii Determination

W. Nörtershäuser,<sup>1,2</sup> R. Sánchez,<sup>1,2</sup> G. Ewald,<sup>1</sup> A. Dax,<sup>1,\*</sup> J. Behr,<sup>3</sup> P. Bricault,<sup>3</sup> B. A. Bushaw,<sup>4</sup> J. Dilling,<sup>3</sup> M. Dombisky,<sup>3</sup> G. W. F. Drake,<sup>5</sup> S. Götze,<sup>1</sup> H.-J. Kluge,<sup>1</sup> Th. Kühl,<sup>1</sup> J. Lassen,<sup>3</sup> C. D. P. Levy,<sup>3</sup> K. Pachucki,<sup>6</sup> M. Pearson,<sup>3</sup> M. Puchalski,<sup>6</sup> A. Wojtaszek,<sup>1,†</sup> Z.-C. Yan,<sup>7</sup> and C. Zimmermann<sup>8</sup>

<sup>1</sup>*GSI Helmholtzzentrum für Schwerionenforschung GmbH, D-64291 Darmstadt, Germany*

<sup>2</sup>*Institut für Kernchemie, Universität Mainz, D-55099 Mainz, Germany*

<sup>3</sup>*TRIUMF, Vancouver, BC, Canada V6T 2A3*

<sup>4</sup>*Pacific Northwest National Laboratory, Richland, WA 99352, USA*

<sup>5</sup>*Department of Physics, University of Windsor, Windsor, Ontario, Canada, N9B 3P4*

<sup>6</sup>*Institute of Theoretical Physics, University of Warsaw, 00-681 Warsaw, Poland*

<sup>7</sup>*Department of Physics, University of New Brunswick, Fredericton, New Brunswick, Canada E3B 5A3*

<sup>8</sup>*Physikalisches Institut, Universität Tübingen, D-72076 Tübingen, Germany*

(Date textdate; Received textdate; Revised textdate; Accepted textdate; Published textdate)

Changes in the mean-square nuclear charge radii along the lithium isotopic chain were determined using a combination of precise isotope shift measurements and theoretical atomic structure calculations. Nuclear charge radii of light elements are of high interest due to the appearance of the nuclear halo phenomenon in this region of the nuclear chart. During the past years we have developed a new laser spectroscopic approach to determine the charge radii of lithium isotopes which combines high sensitivity, speed, and accuracy to measure the extremely small field shift of an 8 ms lifetime isotope with production rates on the order of only 10 000 atoms/s. The method was applied to all bound isotopes of lithium including the two-neutron halo isotope  ${}^{11}\text{Li}$  at the on-line isotope separators at GSI, Darmstadt, Germany and at TRIUMF, Vancouver, Canada. We describe the laser spectroscopic method in detail, present updated and improved values from theory and experiment, and discuss the results.

PACS numbers: 21.10.Gv, 21.10.Ft, 27.20.+h, 32.10.Fn

Keywords: lithium, laser spectroscopy, nuclear charge radius, halo nucleus

## I. INTRODUCTION

Laser spectroscopy of lithium isotopes has recently attracted much interest. This is for two reasons: First, as a three-electron system it can be used to test the fundamental theoretical description of few-electron systems at high accuracy. Second, the extraction of nuclear charge radii from isotope shifts for very light elements became possible by combining high-accuracy measurements with atomic theory. These charge radii are of special interest since one of the lithium isotopes,  ${}^{11}\text{Li}$ , is the best investigated halo nucleus, but a nuclear-model-independent value of its charge radius was not known until recently. Our ToPLiS<sup>1</sup> Collaboration succeeded in measuring the charge radii of all lithium isotopes [1–3]. Here we will describe the experimental setup in detail and discuss the results, including updated and improved values from theory and experiment.

Laser spectroscopy has considerably contributed to our knowledge of ground-state properties of short-lived isotopes. Information on nuclear spins, charge radii, magnetic dipole moments and spectroscopic electric

quadrupole moments can be extracted from isotope shift and hyperfine structure measurements in atomic transitions. A particular strength of these methods is that they provide nuclear-model-independent data. This field has been regularly reviewed, see, *e.g.*, [4–7] within the last decades. While nuclear moments can be obtained with laser spectroscopy from the lightest to the heaviest elements, it was so far not possible to determine nuclear charge radii for short-lived isotopes lighter than neon [8, 9].

The reason is that the isotope shift, in which the charge radius information is encoded, has two contributions: One is the change in nuclear mass between two isotopes (mass shift, MS) and the second one is the difference in the charge distribution inside the nucleus (volume shift or field shift, FS). The MS by far dominates the isotope shift in light elements and then decreases rapidly approximately with increasing mass number  $A$  by  $A^{-2}$ . By contrast, the FS is more than 10 000 times smaller than the MS in the case of the lithium isotopes but increases in proportion to  $Z^2 A^{-1/3}$  with the nuclear charge number  $Z$  and by far exceeds the MS in heavy elements. Separating the tiny FS in the light elements is a complicated task and could only be performed on very simple and stable atoms or ions containing not more than two electrons. The general approach is a very accurate calculation of parts contributing to the mass shift and the comparison with the experimentally observed isotope shift,

\*Current address CERN, CH-1211 Geneva 23, Switzerland.

†Current address Instytut Fizyki, Akademia Swietokrzyska w Kielcach, PL-25-406, Kielce, Poland.

<sup>1</sup> **Two-Photon Lithium Spectroscopy**

as first demonstrated in 1993 for the case of helium by Drake [10]. The difference between these values is then attributed to the change in the nuclear charge radius. Consequently, relative accuracy better than  $10^{-5}$  must be reached in experiment as well as in atomic structure calculations. Here, the correlations in the atom between more than two electrons were an unresolved task. Therefore until a few years ago, this was only possible for one- and two-electron systems, and this approach was used for the stable isotopes of hydrogen [11, 12], helium [10, 13], and  $\text{Li}^+$  [14].

The extension of such measurements to short-lived isotopes was a challenge. The excitation and detection scheme used for measuring isotope shifts in the lithium isotope chain must provide both high efficiency, because  $^{11}\text{Li}$  is produced with production rates of only a few thousand atoms/s, and high resolution and accuracy for extraction of the tiny field shift contribution. Furthermore, it must be a rapid technique since  $^{11}\text{Li}$  is the shortest-lived isotope ( $T_{1/2} = 8$  ms) that has ever been addressed with cw lasers as required for the necessary accuracy<sup>2</sup>. To probe the nuclear charge radius, a transition out of the atomic ground state of lithium seems to be the natural choice. Resonance spectroscopy in the triplet system of the  $\text{Li}^+$  system [14] could in principle be performed as well, but the preparation of such a metastable state is usually quite inefficient and therefore not appropriate. Spectroscopy on trapped ions or atoms has proved to provide the required sensitivity and accuracy for such measurements [16, 17]; however, the  $^{11}\text{Li}$  lifetime is much too short to allow sufficient time for trapping and cooling. The  $2s\ ^2\text{S}_{1/2} \rightarrow 2p\ ^2\text{P}_J$  transitions in Li were used previously for several investigations of  $^{8,9,11}\text{Li}$  in collinear laser spectroscopy by optical pumping and  $\beta$ -NMR detection [18–22]. In these cases the lithium ions, provided by the ISOLDE radioactive beam facility at CERN, were neutralized in flight in a charge exchange cell and then used as a fast atomic beam. However, the Doppler shift of the transition frequency due to the beam velocity of the accelerated ions, and the limited knowledge of the acceleration voltage with an uncertainty of typically  $10^{-4}$  is prohibitive for isotope shift measurements. Recently, such measurements became practicable for  $\text{Be}^+$  ions by using a frequency comb and simultaneous spectroscopy in parallel and antiparallel direction [23, 24] in order to eliminate voltage uncertainties. Those studies are still limited by statistical and systematic uncertainties to an accuracy of about 1 MHz, which is not sufficient for lithium isotopes. Hence, in the experiment discussed here, the  $\text{Li}^+$  ions are stopped and neutralized before spectroscopy is performed on the atomic cloud. To avoid large Doppler broadening, the  $2s\ ^2\text{S}_{1/2} \rightarrow 3s\ ^2\text{S}_{1/2}$  two-photon transi-

tion is studied, which is to first order Doppler-free.

After a series of short letters [1–3, 25] in which we reported results on the charge radii of all isotopes, we describe here in detail the experimental technique as well as the theoretical calculations and discuss all possible sources of systematic uncertainties that were further studied. The paper is organized as follows: In Section II we give a summary of the theoretical mass shift calculations that were performed and steadily improved during the last years, including relativistic, QED and nuclear structure corrections. Afterwards, the experimental setup is described, including radioactive beam production, separation and the transformation into a thermal atomic beam. Resonance ionization mass spectroscopy is combined with two-photon spectroscopy to reach the required accuracy and efficiency simultaneously. The corresponding results and the change in nuclear charge radius for the pair of stable isotopes  $^{6,7}\text{Li}$  are presented in Section IV. Results for the stable isotopes are compared with other experimental data obtained by optical spectroscopy of the lithium ion or atom to verify the consistency of the data. The paper closes with the presentation of the extracted changes in the mean-square (ms) nuclear charge radii  $\delta \langle r^2 \rangle^{6,A}$  relative to the reference isotope  $^6\text{Li}$ . These values can be extracted independently from further information in a model-independent way [4].

Most interesting for nuclear-structure studies are absolute nuclear charge or nuclear matter radii. To determine charge radii from our isotope shift measurements, we need the nuclear charge radius of at least one reference isotope obtained by a different technique. A nuclear charge radius determination solely based on optical measurements of the absolute transition frequency and atomic theory calculations is thus far only possible for hydrogen [26]. Experimental data are now in principle also available for the lithium isotopes [27]; however, atomic theory for three-electron atoms is not yet able to achieve absolute transition frequencies sufficiently accurate to extract the  $10^{-9}$  contribution of the finite nuclear size effect. The choice of the reference isotope and the respective charge radii together with an evaluation of theoretical results will be discussed in a following publication [28].

## II. THEORY

To extract nuclear charge radii from isotope shift measurements of the lightest elements, calculations of the mass-dependent part of the isotope shift at the highest level that is currently achievable are required. In this Section we will present the latest results for the lithium isotopes. The calculation starts with constructing the solution of the nonrelativistic Schrödinger equation using variational calculations in Hylleraas coordinates. These solutions are then the basis for the calculation of relativistic and quantum electrodynamic contributions. Finally, nuclear structure corrections are included. The

<sup>2</sup> Only some radioisotopes of americium, investigated by the group of H. Backe [15], have even shorter half lives but here broad-band pulsed lasers could be applied.

finite nuclear size effect is actually the part that will be extracted from experiment. But the proportionality coefficient between the change in the mean-square nuclear charge radius and the extracted nuclear volume effect in the isotope shift has to be provided by theory. Additionally, as with many halo nuclei, the  $^{11}\text{Li}$  nucleus possesses strong electric dipole transitions to low-lying states, making it a so-called “soft-dipole” with a relatively large nuclear polarizability compared with less exotic nuclei. The influence of this polarizability on the atomic electron levels was recently evaluated [29] and leads to a significant contribution. In the following Sections, the details of the atomic structure calculations will be explained.

### A. General Approach

In order to extract the rms nuclear charge radius from the measured isotope shift, we begin by writing the isotope shift for an atomic transition  $a \rightarrow b$  between isotopes  $A$  and  $A'$  in the form

$$\begin{aligned} \delta\nu_{a \rightarrow b}^{A,A'} &= \nu_{a \rightarrow b}^{A'} - \nu_{a \rightarrow b}^A \\ &= \delta\nu_{a \rightarrow b}^{(0)}(A, A') + C_{a \rightarrow b}[\bar{r}_c^2(A') - \bar{r}_c^2(A)] \end{aligned} \quad (1)$$

$$\delta\nu_{\text{IS}}^{A,A'} = \delta\nu_{\text{MS}}^{A,A'} + C_{A,A'} \cdot \delta\langle r^2 \rangle^{A,A'}, \quad (2)$$

where  $\bar{r}_c(A)$  and  $\bar{r}_c(A')$  are the rms charge radii for the two isotopes, and the remaining term  $\delta\nu_{a \rightarrow b}^{(0)}(A, A')$  comes from the mass dependence of the atomic energy levels. Hence, it is called the mass shift (MS). As will be seen, the coefficient  $C_{a \rightarrow b}$  is nearly independent of the isotopes involved, but in the case of lithium, relativistic corrections to the wave function at the origin and leading recoil corrections should be included [30]. The main challenge is to calculate the term  $\delta\nu_{a \rightarrow b}^{(0)}(A, A')$  to sufficient accuracy. Equation (1) can be written in the form (2) that usually appears in experimental papers, where the particular transition index is suppressed. Here, the mass-shift and the  $\delta\langle r^2 \rangle^{A,A'}$  dependence of the field shift are clearly stated. In the following, we will always refer to the  $2s^2\text{S}_{1/2} \rightarrow 3s^2\text{S}_{1/2}$  two-photon transition.

To give an overview of the contributions to  $\delta\nu_{\text{MS}}^{A,A'}$ , it is convenient to arrange them in the form of a double series expansion in powers of  $\alpha \simeq 1/137.036$  and the electron reduced-mass-to-nuclear-mass ratio  $\mu/M \simeq 10^{-4}$ , where  $\mu = mM/(m+M)$ . Table I summarizes the various contributions, including the QED corrections and the finite nuclear size term. Since all the lower-order terms can now be calculated to very high accuracy, including the QED terms of order  $\alpha^3 \text{Ry}$ , the dominant source of uncertainty comes from the QED corrections of order  $\alpha^4 \text{Ry}$  or higher. For the isotope shift, the QED terms independent of  $\mu/M$  cancel, and so it is only the radiative recoil terms of order  $\alpha^4 \mu/M \simeq 10^{-12} \text{Ry}$  ( $\sim 10 \text{ kHz}$ ) that contribute to the uncertainty. Since this is much less than the finite nuclear size correction of about  $1 \text{ MHz}$ , the

TABLE I: Contributions to the energy in units of the Rydberg constant and their leading orders of magnitude in terms of  $Z$ ,  $\mu/M \sim 10^{-4}$ , and  $\alpha \sim 10^{-2}$ .  $\alpha_{\text{d,nuc}}$  is the nuclear dipole polarizability and  $a_0$  the Bohr atomic radius.

Contribution	Magnitude
Nonrelativistic energy	$Z^2$
Mass polarization	$Z^2 \mu/M$
Second-order mass polarization	$Z^2 (\mu/M)^2$
Relativistic corrections	$Z^4 \alpha^2$
Relativistic recoil	$Z^4 \alpha^2 \mu/M$
Anomalous magnetic moment	$Z^4 \alpha^3$
Hyperfine structure	$Z^3 g_I \mu_0^2$
Lamb shift	$Z^4 \alpha^3 \ln \alpha + \dots$
Radiative recoil	$Z^4 \alpha^3 (\ln \alpha) \mu/M$
Finite nuclear size	$Z^4 \langle \bar{r}_c / a_0 \rangle^2$
Finite size recoil	$Z^4 \mu/M \langle r_c / a_0 \rangle^2$
Nuclear polarization	$Z^3 e^2 \alpha_{\text{d,nuc}} / (\alpha a_0)$

comparison between theory and experiment clearly provides a means to determine the nuclear size. This is the key point to keep in mind when considering the theoretical contributions to the isotope shift.

### B. Solution to the Nonrelativistic Schrödinger Equation

The foundation for the calculation, and the subsequent evaluation of relativistic and QED corrections, is to find high-precision solutions to the nonrelativistic Schrödinger equation for finite nuclear mass. The past 20 years have seen important advances in developing specialized techniques for doing this in the case of the three-body problem (helium-like systems) [10, 31, 32], and more recently the four-body problem [29, 33–36]. The usual methods of theoretical atomic physics, such as the Hartree-Fock approximation or configuration interaction methods, are not capable of yielding results of spectroscopic accuracy, and so specialized techniques of the type used here are needed.

For convenience, we begin by rescaling distances according to  $r \rightarrow (m/\mu)r$ . The advantage gained is that the Hamiltonian for a three-electron atomic system can then be written in the form

$$H = H_0 + \lambda H_{\text{MP}}, \quad (3)$$

with

$$H_0 = -\frac{1}{2} \sum_{i=1}^3 \nabla_i^2 - Z \sum_{i=1}^3 \frac{1}{r_i} + \sum_{i>j}^3 \frac{1}{r_{ij}}, \quad (4)$$

and

$$H_{\text{MP}} = \sum_{i>j}^3 \nabla_i \cdot \nabla_j, \quad (5)$$

in units of  $2R_M$ , where the Rydberg constant for finite nuclear mass is defined by  $R_M = (1 - \mu/M)R_\infty$ , and  $\lambda = -\mu/M$  can be treated as a perturbation parameter. The Schrödinger equation

$$H\Psi = E\Psi \quad (6)$$

was solved perturbatively by expanding  $\Psi$  and  $E$  accordingly to

$$\Psi = \Psi_0 + \lambda\Psi_1 + \dots, \quad (7)$$

$$E = \varepsilon_0 + \lambda\varepsilon_1 + \lambda^2\varepsilon_2 + \dots. \quad (8)$$

Thus Eq. (6) becomes

$$H_0\Psi_0 = \varepsilon_0\Psi_0, \quad (9)$$

$$(\varepsilon_0 - H_0)\Psi_1 = (H_{\text{MP}} - \varepsilon_1)\Psi_0. \quad (10)$$

$\varepsilon_1$  and  $\varepsilon_2$  are

$$\varepsilon_1 = \langle \Psi_0 | H_{\text{MP}} | \Psi_0 \rangle, \quad (11)$$

$$\varepsilon_2 = \langle \Psi_0 | H_{\text{MP}} | \Psi_1 \rangle - \varepsilon_1 \langle \Psi_0 | \Psi_1 \rangle. \quad (12)$$

Both  $\Psi_0$  and  $\Psi_1$  were solved variationally in multiple basis sets in Hylleraas coordinates containing terms of the form

$$r_1^{j_1} r_2^{j_2} r_3^{j_3} r_{12}^{j_{12}} r_{23}^{j_{23}} r_{31}^{j_{31}} e^{-\alpha_p r_1 - \beta_p r_2 - \gamma_p r_3} \times \mathcal{Y}_{(\ell_1 \ell_2) \ell_{12}, \ell_3}^{LM}(\mathbf{r}_1, \mathbf{r}_2, \mathbf{r}_3) \chi_1, \quad (13)$$

where  $\mathcal{Y}_{(\ell_1 \ell_2) \ell_{12}, \ell_3}^{LM}$  is a vector-coupled product of spherical harmonics for the three electrons to form a state of total angular momentum  $L$ , and  $\chi_1$  is a spin function with spin angular momentum  $1/2$ .

As described previously [37, 38], the basis set is divided into five sectors with different values of the scale factors  $\alpha_p$ ,  $\beta_p$ , and  $\gamma_p$  in each sector, as labelled by the subscript  $p$ . The 15 independent scale factors are then optimized by a global minimization of the energy. Except for restrictions on which correlation terms are included in each sector (see Ref. [38]), all terms from (13) are included such that

$$j_1 + j_2 + j_3 + j_{12} + j_{23} + j_{31} \leq \Omega, \quad (14)$$

and the convergence of the eigenvalues is studied as  $\Omega$  is progressively increased. Further details may be found in Ref. [38]. Since Eq. (8) is expressed in units of  $(1 + \lambda) 2R_\infty$ , the explicit mass-dependence of  $E$  in units of  $2R_\infty$  is

$$E = \varepsilon_0 + \lambda(\varepsilon_0 + \varepsilon_1) + \lambda^2(\varepsilon_1 + \varepsilon_2) + O(\lambda^3). \quad (15)$$

### C. Relativistic and Relativistic Recoil Corrections

The lowest-order relativistic corrections of  $O(\alpha^2)$  and the spin-dependent anomalous magnetic moment corrections of  $O(\alpha^3)$  can be written in the form [31, 39] (in atomic units)

$$E_{\text{rel}} = \langle \Psi | H_{\text{rel}} | \Psi \rangle_J, \quad (16)$$

where  $\Psi$  is a nonrelativistic wave function and  $H_{\text{rel}}$  is defined by

$$\begin{aligned} H_{\text{rel}} = & B_1 + B_2 + B_{3e} + B_{3z} + B_5 \quad (17) \\ & - \pi\alpha^2 \sum_{i>j}^3 \left( 1 + \frac{8}{3} \mathbf{s}_i \cdot \mathbf{s}_j \right) \delta(\mathbf{r}_{ij}) + \\ & \frac{1}{2} Z\pi\alpha^2 \sum_{i=1}^3 \delta(\mathbf{r}_i) + \frac{m}{M} (\tilde{\Delta}_2 + \tilde{\Delta}_{3z}) \\ & + \gamma \left( 2B_{3z} + \frac{4}{3} B_{3e} + \frac{2}{3} B_{3e}^{(1)} + 2B_5 \right) \\ & + \gamma \frac{m}{M} \tilde{\Delta}_{3z}. \end{aligned}$$

In (17),

$$B_1 = -\frac{\alpha^2}{8} (\nabla_1^4 + \nabla_2^4 + \nabla_3^4), \quad (18)$$

$$B_2 = \frac{\alpha^2}{2} \sum_{i>j}^3 \left[ \frac{1}{r_{ij}} \nabla_i \cdot \nabla_j + \frac{1}{r_{ij}^3} \mathbf{r}_{ij} \cdot (\mathbf{r}_{ij} \cdot \nabla_i) \nabla_j \right], \quad (19)$$

$$B_{3e} = \frac{\alpha^2}{2} \sum_{i \neq j}^3 \frac{1}{r_{ij}^3} \mathbf{r}_{ji} \times \mathbf{p}_i \cdot (\mathbf{s}_i + 2\mathbf{s}_j), \quad (20)$$

$$B_{3z} = \frac{Z\alpha^2}{2} \sum_{i=1}^3 \frac{1}{r_i^3} \mathbf{r}_i \times \mathbf{p}_i \cdot \mathbf{s}_i, \quad (21)$$

$$B_5 = \alpha^2 \sum_{i>j}^3 \left[ \frac{1}{r_{ij}^3} (\mathbf{s}_i \cdot \mathbf{s}_j) - \frac{3}{r_{ij}^5} (\mathbf{r}_{ij} \cdot \mathbf{s}_i) (\mathbf{r}_{ij} \cdot \mathbf{s}_j) \right], \quad (22)$$

$$\tilde{\Delta}_2 = \frac{iZ\alpha^2}{2} \sum_{j=1}^3 \left[ \frac{1}{r_j} \mathbf{p} \cdot \nabla_j + \frac{1}{r_j^3} \mathbf{r}_j \cdot (\mathbf{r}_j \cdot \mathbf{p}) \nabla_j \right], \quad (23)$$

$$\tilde{\Delta}_{3Z} = Z\alpha^2 \sum_{i=1}^3 \frac{1}{r_i^3} \mathbf{r}_i \times \mathbf{p} \cdot \mathbf{s}_i, \quad (24)$$

$$B_{3e}^{(1)} = \frac{\alpha^2}{2} \sum_{i \neq j}^3 \frac{1}{r_{ij}^3} \mathbf{r}_{ji} \times \mathbf{p}_i \cdot (\mathbf{s}_i - \mathbf{s}_j), \quad (25)$$

with  $\mathbf{p} = \mathbf{p}_1 + \mathbf{p}_2 + \mathbf{p}_3$ , and  $\gamma$  is

$$\gamma = \frac{\alpha}{2\pi} + (-0.32847) \left( \frac{\alpha}{\pi} \right)^2 + \dots. \quad (26)$$

The operator  $-\pi\alpha^2 \sum_{i>j} (1 + \frac{8}{3} \mathbf{s}_i \cdot \mathbf{s}_j) \delta(\mathbf{r}_{ij})$  can be replaced by  $\pi\alpha^2 \sum_{i>j} \delta(\mathbf{r}_{ij})$  and the expectation value of

the spin-spin term  $B_5$  vanishes. The terms proportional to  $m/M$  are the nuclear relativistic recoil corrections and the terms proportional to  $\gamma$  are the anomalous magnetic moment corrections.

The perturbing effect of mass polarization on the expectation values of Breit operators can be obtained using

$$\Psi = \Psi_0 + \lambda(\Psi_1 - \langle \Psi_1 | \Psi_0 \rangle \Psi_0) + \dots, \quad (27)$$

where the extra term  $-\langle \Psi_1 | \Psi_0 \rangle \Psi_0$  is added to  $\Psi_1$  so that the first two terms of the right hand side are orthogonal to each other [40]. Thus, for a Breit operator  $A$ , one has

$$\langle \Psi | A | \Psi \rangle = a_0 + \lambda a_1 + \dots, \quad (28)$$

where

$$a_0 = \langle \Psi_0 | A | \Psi_0 \rangle, \quad (29)$$

and

$$a_1 = 2\langle \Psi_0 | A | \Psi_1 \rangle - 2\langle \Psi_0 | \Psi_1 \rangle \langle \Psi_0 | A | \Psi_0 \rangle. \quad (30)$$

Furthermore, due to the use of  $\mu$ -scaled atomic units in Eq. (3), the units of  $\langle \Psi | A | \Psi \rangle$  in Eq. (28) are  $(\mu/m)^n 2R_\infty$ , where  $-n$  is the degree of homogeneity of operator  $A$  in the three-electron coordinate space such that

$$A(\beta \mathbf{r}_1, \beta \mathbf{r}_2, \beta \mathbf{r}_3) = \beta^{-n} A(\mathbf{r}_1, \mathbf{r}_2, \mathbf{r}_3). \quad (31)$$

Using

$$\left(\frac{\mu}{m}\right)^n = (1 + \lambda)^n \approx 1 + n\lambda, \quad (32)$$

one has the explicit mass-dependent formula

$$\langle \Psi | A | \Psi \rangle = a_0 + \lambda(na_0 + a_1) + O(\lambda^2), \quad (33)$$

in units of  $2R_\infty$ .

#### D. QED Corrections

Until recently, the QED contributions of lowest order  $\alpha^3 \text{Ry}$  were the major source of uncertainty in calculations of atomic energy levels and the isotope shift for atoms more complicated than hydrogen. However, tremendous progress has been made in recent years. Complete results to lowest order  $\alpha^3 \text{Ry}$  are now readily obtainable, and higher order corrections can be estimated in a screened hydrogenic approximation. For a many-electron atom, it is convenient to express the total QED shift in the form

$$E_{\text{QED}} = E_{L,1} + E_{M,1} + E_{R,1} + E_{L,2}, \quad (34)$$

where  $E_{L,1}$  is the mass-independent part of the electron-nucleus Lamb shift (the Kabir-Salpeter term [41]),  $E_{M,1}$  contains mass scaling and mass polarization corrections,

$E_{R,1}$  contains recoil corrections (including radiative recoil), and  $E_{L,2}$  is the electron-electron term originally obtained by Araki [42] and Sucher [43]. We now discuss each of these in turn.

The term  $E_{L,1}$  closely resembles the corresponding hydrogenic Lamb shift [44], except that an overall multiplying factor of  $\langle \delta(\mathbf{r}) \rangle = Z^3 \delta_{L,0} / (\pi n^3)$  for the hydrogenic case is replaced by the correct expectation value  $\langle \sum_{j=1}^N \delta(\mathbf{r}_j) \rangle$  for the multi-electron case, summed over the  $N$  electrons. The residual state dependence due to other terms such as the Bethe logarithm discussed below is then relatively weak.

Following the notation of Eq. (3) for the mass polarization corrections, the main electron-nucleus part for infinite nuclear mass is (in atomic units throughout)

$$\begin{aligned} E_{L,1} = & \frac{4Z\alpha^3 \langle \delta(\mathbf{r}_i) \rangle^{(0)}}{3} \left\{ \ln(Z\alpha)^{-2} - \beta(n^2 L) + \frac{19}{30} \right. \\ & + (3\pi\alpha Z)0.765405577 \\ & + \frac{\alpha}{\pi} [0.40417 - (3\alpha Z/4)21.55685] \\ & + (Z\alpha)^2 \left[ -\frac{3}{4} \ln^2(Z\alpha)^{-2} + C_{61}(1s^x nL) \ln(Z\alpha)^{-2} \right. \\ & \left. \left. + C_{60}(1s^x nL) \right] \right\}, \quad (35) \end{aligned}$$

the mass scaling and mass polarization corrections are

$$\begin{aligned} E_{M,1} = & \frac{\mu \langle \delta(\mathbf{r}_i) \rangle^{(1)}}{M \langle \delta(\mathbf{r}_i) \rangle^{(0)}} E_{L,1} \\ & + \frac{4Z\alpha^3 \mu \langle \delta(\mathbf{r}_i) \rangle^{(0)}}{3M} [1 - \Delta\beta_{\text{MP}}(n^2 L)], \quad (36) \end{aligned}$$

and the recoil corrections (including radiative recoil) are given by

$$\begin{aligned} E_{R,1} = & \frac{4Z^2 \alpha^3 \mu \langle \delta(\mathbf{r}_i) \rangle^{(0)}}{3M} \left[ \frac{1}{4} \ln(Z\alpha)^{-2} - 2\beta(n^2 L) - \frac{1}{12} \right. \\ & - \frac{7}{4} a(1s^x nL) - \frac{3}{4} (\pi\alpha)1.36449 \\ & \left. + \frac{3}{4} \pi Z \alpha D_{50}(n^2 L) + \frac{1}{2} \alpha^2 Z \ln^2(Z\alpha)^{-2} \right]. \quad (37) \end{aligned}$$

These equations involve contributions to the hydrogenic Lamb shift obtained by many authors, as summarized by Eides *et al.* [44]. The quantity  $\beta(1s^x nL) = \ln(k_0/Z^2 R_\infty)$  is the two- or three-electron Bethe logarithm, and the two terms  $1 - \Delta\beta_{\text{MP}}(1s^x nL)$  in Eq. (36) account for the mass scaling and mass polarization corrections to  $\beta(1s^x nL)$  respectively. These terms are further discussed below. The term  $a(1s^x nL)$  is a well-known part of the hydrogenic Lamb shift. Its many-electron generalization is given by [34, 45, 46]

$$a(1s^x nL) = \frac{2Q_1^{(0)}}{\sum_{j=1}^N \langle \delta(\mathbf{r}_j) \rangle} - 3, \quad (38)$$

where

$$Q_1^{(0)} = \frac{1}{4\pi} \lim_{\epsilon \rightarrow 0} \sum_j \langle r_j^{-3}(\epsilon) + 4\pi(\gamma + \ln \epsilon) \delta(\mathbf{r}_j) \rangle. \quad (39)$$

$\gamma$  is Euler's constant and  $\epsilon$  is the radius of a sphere about  $r_j = 0$  that is excluded from the integration.

The orders of magnitude for the other state-dependent coefficients  $C_{61}(1s^x nL)$ ,  $C_{60}(1s^x nL)$ , and  $D_{50}(1s^x nL)$  are all estimated from the generic formula

$$X(1s^x nL) = \frac{x\tilde{X}(1s) + \tilde{X}(nL)/n^3}{x + \delta_{L,0}/n^3}, \quad (40)$$

where  $\tilde{X}(nL)$  is the corresponding one-electron coefficient, evaluated directly with the full nuclear charge  $Z$  for  $L = 0$  and with a fully screened nuclear charge  $Z - x$  for the outer  $nL$  electron for  $L > 0$  [47]. The numerical values can be immediately calculated from the hydrogenic values, as discussed by Drake and Martin [47] for helium, and Yan and Drake [34] for lithium. Their contribution to the transition energy is taken to be the QED uncertainty.

The electron-electron QED shift  $E_{L,2}$  can similarly be separated into mass-independent and mass-dependent parts according to

$$E_{L,2} = E_{L,2}^{(0)} + \frac{\mu}{M} E_{L,2}^{(1)} + \dots, \quad (41)$$

where

$$E_{L,2}^{(0)} = \alpha^3 \left( \frac{14}{3} \ln \alpha + \frac{164}{15} \right) \sum_{i>j} \langle \delta(\mathbf{r}_{ij}) \rangle^{(0)} - \frac{14}{3} \alpha^3 Q^{(0)}, \quad (42)$$

and the mass scaling and mass polarization corrections are

$$E_{L,2}^{(1)} = -3E_{L,2}^{(0)} + \alpha^3 \left( \frac{14}{3} \ln \alpha + \frac{164}{15} \right) \sum_{i>j} \langle \delta(\mathbf{r}_{ij}) \rangle^{(1)} - \frac{14}{3} \alpha^3 \left( Q^{(1)} + \sum_{i>j} \langle \delta(\mathbf{r}_{ij}) \rangle^{(0)} \right). \quad (43)$$

Following our notation, the  $Q^{(0)}$ -term for infinite mass is given by

$$Q^{(0)} = \frac{1}{4\pi} \lim_{\epsilon \rightarrow 0} \sum_{i>j} \langle r_{ij}^{-3}(\epsilon) + 4\pi(\gamma + \ln \epsilon) \delta(\mathbf{r}_{ij}) \rangle. \quad (44)$$

The  $Q^{(1)}$  term is the correction due to the mass polarization correction to the wave function. As a word of explanation, the infinitesimal limiting quantity  $\epsilon$  has dimensions of distance, and so it generates an additional finite mass correction when distances are rescaled for the finite mass case according to  $\epsilon \rightarrow (\mu/m)\epsilon$ .

The principal computational challenge is the calculation of the Bethe logarithm  $\beta(1s^2 nL)$  in  $E_{L,1}$ , originating from the emission and re-absorption of a virtual photon, and the finite mass correction  $\Delta\beta_{\text{MP}}(1s^2 nL)$  due to mass polarization. The Bethe logarithm is the logarithmic re-

TABLE II: Comparison of Bethe logarithms for lithium and its ions.

Atom	Li(1s <sup>2</sup> 2s)	Li(1s <sup>2</sup> 3s)	Li <sup>+</sup> (1s <sup>2</sup> )	Li <sup>++</sup> (1s)
$\ln(k_0/Z^2 Ry)$	2.981 06(1)	2.982 36(6)	2.982 624	2.984 128

mainder after mass renormalization and is defined by

$$\beta(1s^2 nL) = \frac{\mathcal{N}}{\mathcal{D}} = \quad (45)$$

$$\frac{\sum_i |\langle \Psi_0 | \mathbf{p}_1 + \mathbf{p}_2 | i \rangle|^2 (E_i - E_0) \ln |E_i - E_0|}{\sum_i |\langle \Psi_0 | \mathbf{p}_1 + \mathbf{p}_2 | i \rangle|^2 (E_i - E_0)}.$$

The accurate calculation of  $\beta(1s^2 nL)$  has been a long-standing problem in atomic physics. This has been solved by use of a discrete variational representation of the continuum in terms of pseudostates [48]. The key idea is to define a variational basis set containing a huge range of distance scales through multiple sets of exponential scale factors  $\alpha$  and  $\beta$  that themselves span many orders of magnitude. The Bethe logarithm comes almost entirely from virtual excitations of the inner 1s electron to  $p$ -states lying high in the photoionization continuum, and so the basis set must be extended to very short distances for this particle. The outer electrons are to a good approximation just spectators to these virtual excitations.

Table II compares the Bethe logarithms for the two lowest  $s$ -states of lithium with those for the Li-like ions Li<sup>+</sup>(1s<sup>2</sup> 1S) and Li<sup>++</sup>(1s 2S). The comparison emphasizes that the Bethe logarithm is determined almost entirely by the hydrogenic value for the 1s electron and is rather independent of the state of excitation of the outer electrons or the degree of ionization. In order to make the connection with the hydrogenic Bethe logarithm more obvious, the quantity tabulated is  $\ln(k_0/Z^2 Ry)$ . The effect of dividing by a factor of  $Z^2$  is to reduce all the Bethe logarithms to approximately the same number  $\beta(1s) = 2.984 128 556$  for the ground state of hydrogen.

## E. Nuclear Polarizability

The interaction of the nucleus with an electromagnetic field can be described by the Hamiltonian

$$H_{\text{int}} = q A^0 - \mathbf{d} \cdot \mathbf{E} - \boldsymbol{\mu} \cdot \mathbf{B} - \frac{q}{6} \langle r^2 \rangle \nabla \cdot \mathbf{E}, \quad (46)$$

which is valid as long as the characteristic momentum of the electromagnetic field is smaller than the inverse of the nuclear size. Otherwise, one has to use a complete description in terms of form factors and structure functions. Under this assumption, the dominant term for the nuclear excitation is the electric dipole interaction. This

is the main approximation of this approach, which may not always be valid. It was checked however that higher order polarizabilities are quite small (below 1 kHz) for deuterium [49, 50], and this is similar for He, Li and Be isotopes. Within this low electromagnetic momentum approximation, the nuclear polarizability correction to the energy is given by [29] (in units  $\hbar = c = 1, e^2 = 4\pi\alpha$ )

$$E_{\text{pol}} = -m\alpha^4 \left\langle \sum_a \delta^3(r_a) \right\rangle (m^3 \tilde{\alpha}_{\text{pol}}), \quad (47)$$

where  $m$  is the electron mass and the expectation value of the Dirac  $\delta$  is taken with the electron wave function in atomic units. For hydrogenic systems it is equal to  $Z^3/\pi$ . In the equation above,  $\tilde{\alpha}_{\text{pol}}$  is a *weighted* electric polarizability of the nucleus, which is given by the double integral

$$\begin{aligned} \tilde{\alpha}_{\text{pol}} &= \frac{16\alpha}{3} \int_{E_T}^{\infty} dE \frac{1}{e^2} |\langle \phi_N | \mathbf{d} | E \rangle|^2 \int_0^{\infty} \frac{dw}{w} \frac{E}{E^2 + w^2} \\ &\times \frac{1}{(\kappa + \kappa^*)} \left[ 1 + \frac{1}{(\kappa + 1)(\kappa^* + 1)} \left( \frac{1}{\kappa + 1} + \frac{1}{\kappa^* + 1} \right) \right] \end{aligned} \quad (48)$$

where  $\kappa = \sqrt{1 + 2im/w}$  and  $E_T$  is the excitation energy for the nuclear breakup threshold.

The kets  $|\phi_N\rangle$  and  $|E\rangle$  denote the ground state of the nucleus and a dipole excited state with excitation energy  $E$ , respectively. The square of the dipole moment is related to the so called  $B(E1)$  function by the relation

$$|\langle \phi_N | \mathbf{d} | E \rangle|^2 = \frac{4\pi}{3} \frac{dB(E1)}{dE} \quad (49)$$

in units  $e^2 \text{fm}^2 \text{MeV}^{-1}$ , which explains the presence of  $e^2$  in the denominator in Eq. (48).

If  $E_T$  is much larger than the electron mass  $m$ , one can perform a small electron mass expansion and obtain a simplified formula [51, 52]:

$$\tilde{\alpha}_{\text{pol}} = \frac{19}{6} \alpha_E + 5 \alpha_{E \log} \quad (50)$$

with the static electric dipole polarizability

$$\begin{aligned} \alpha_E &= \frac{2\alpha}{3} \frac{1}{e^2} \left\langle \phi_N \left| \mathbf{d} \frac{1}{H_N - E_N} \mathbf{d} \right| \phi_N \right\rangle \\ &= \frac{8\pi\alpha}{9} \int_{E_T}^{\infty} \frac{dE}{E} \frac{1}{e^2} \frac{dB(E1)}{dE} \end{aligned} \quad (51)$$

and the logarithmically modified polarizability

$$\begin{aligned} \alpha_{E \log} &= \frac{2\alpha}{3} \frac{1}{e^2} \left\langle \phi_N \left| \mathbf{d} \frac{1}{H_N - E_N} \right. \right. \\ &\quad \left. \left. \times \ln \left( \frac{2(H_N - E_N)}{m} \right) \mathbf{d} \right| \phi_N \right\rangle \\ &= \frac{8\pi\alpha}{9} \int_{E_T}^{\infty} \frac{dE}{E} \frac{1}{e^2} \frac{dB(E1)}{dE} \ln \left( \frac{2E}{m} \right). \end{aligned} \quad (52)$$

This approximation is for example valid for  $^3\text{He}$  and  $^4\text{He}$  isotopes, but not for  $^{11}\text{Li}$  or  $^{11}\text{Be}$ .

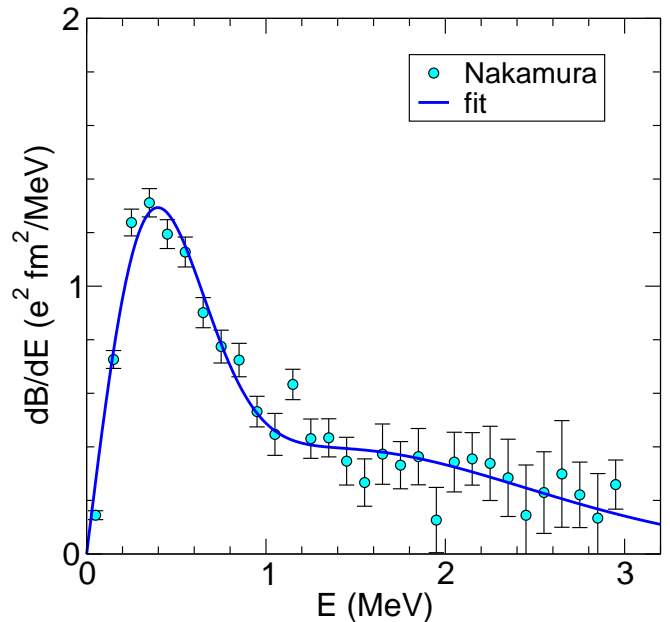


FIG. 1: Electric dipole line strength by Nakamura *et al.* [17] adapted to the new value of  $E_T = 369.15(65)$  keV from [53].

In the opposite situation, i.e., when  $m$  is much larger than  $E_T$ , we can use the nonrelativistic limit, and the polarizability correction adopts the form (with  $m$  being the reduced mass here)

$$\begin{aligned} E_{\text{pol}} &= -m\alpha^4 \left\langle \sum_a \delta^3(r_a) \right\rangle \frac{32\pi\alpha m^2}{9} \\ &\times \int_{E_T}^{\infty} dE \frac{1}{e^2} \frac{dB(E1)}{dE} \sqrt{\frac{m}{2E}}. \end{aligned} \quad (53)$$

This approximation is justified for muonic helium atoms or ions, because the muon mass ( $\sim 106$  MeV) is much larger than the threshold energy  $E_T = 369.15(65)$  keV [53]. This formula requires, however, a few significant corrections, namely Coulomb distortion and form factor corrections. They were obtained by Friar in [54] for the calculation of the polarizability correction in  $\mu^4\text{He}$ . This nonrelativistic approximation, however, is not valid for electronic atoms since the typical nuclear excitation energy in light nuclei is larger than the electron mass. This indicates a possible limitation in the comparison of charge radii obtained from electronic and muonic atoms, as the nuclear structure effects are much different.

The  $B(E1)$  function is directly related to the photoabsorption cross Section at photon energies  $E$

$$\sigma(E) = \frac{16\pi^3}{9} \alpha E \left( \frac{1}{e^2} \frac{dB(E1)}{dE} \right), \quad (54)$$

which allows us to obtain the  $B(E1)$  function from experimental data presented in [17] and shown in Fig. 1. With the two-neutron separation energy  $E_T = 369.15(65)$  keV

from [53] one obtains

$$\tilde{\alpha}_{\text{pol}} = 60.9(6.1) \text{ fm}^{-3} = 1.06(0.11) 10^{-6} \lambda_C^3, \quad (55)$$

and a polarizability correction to the  $2s \ ^2S_{1/2} \rightarrow 3s \ ^2S_{1/2}$  transition frequency of  $\nu_{\text{pol}} = 39(4) \text{ kHz}$ . The polarizability correction for the lighter lithium isotopes is expected to be negligible due to much larger separation energies.

### F. Extraction of Nuclear Charge Radii

The various contributions to the isotope shift as they have been discussed so far are listed in Table III for all lithium isotopes relative to  $^6\text{Li}$ . The mass values that were used for the calculations are also included for reference. In addition, there is a significant electronic binding energy correction  $\Delta M = -E_{\text{binding}}/c^2$ . The terms are classified according to their dependence on  $\mu/M$  and the fine structure constant  $\alpha$ . As an important check, most of the results have been calculated independently by Puchalski and Pachucki (P&P) in Poland [57], and by Yan and Drake (Y&D) in Canada [58]. Two exceptions are the Bethe logarithm part of the radiative recoil correction, which have been calculated only by Y&D [58], and the nuclear polarizability correction, which has been calculated only by P&P [29]. In some cases, the two sets of results are slightly different due to different methods of calculation, as noted in the table. In these cases, both sets of results are given for comparison. The differences are not large enough to affect the determination of the nuclear charge radius from experimental results, but they indicate the areas where further work is desirable.

The various contributions are as follows: The term labelled  $\mu/M$  contains the sum of the reduced mass scaling of the nonrelativistic ionization energy, and the first-order mass polarization correction. For example, the mass-scaling term is  $2R_\infty[E_{\text{NR}}(\text{Li}^+, \infty) - E_{\text{NR}}(\text{Li}, \infty)][(\mu/M)_{A\text{Li}} - (\mu/M)_{6\text{Li}}]$ , where  $E_{\text{NR}}(\text{Li}, \infty)$  is the nonrelativistic energy for infinite nuclear mass (in atomic units), and  $R_\infty$  is the corresponding Rydberg constant.

The term of order  $(\mu/M)^2$  comes from second-order mass polarization. The relativistic recoil terms of order  $\alpha^2\mu/M$  results from mass scaling, mass polarization, and the Stone terms as expressed by Eqs. (23) and (24). The two sets of results here do not quite agree because the Y&D results include partial contributions from the next-higher-order terms of order  $\alpha^2(\mu/M)^2$ . The difference between the two calculations is an indication of the uncertainty due to the partial neglect of these higher-order terms. The numbers in this row are anomalously small because of nearly complete numerical cancellation between the mass polarization and mass scaling plus Stone contributions. For example, for the case of  $^{11}\text{Li}$ , the two parts are  $-17.9198(4) \text{ MHz}$  and  $+17.9735 \text{ MHz}$ , respectively, resulting in a final recoil term of only  $0.0537(4) \text{ MHz}$ . Because of this cancellation, the percentage uncertainty is relatively large.

The radiative recoil terms of order  $\alpha^3\mu/M$  similarly come from a combination of mass scaling, mass polarization, and higher-order recoil corrections, as discussed in [29, 33–36, 58, 59]. The most difficult part of the calculation is the Bethe logarithm contribution obtained in Ref. [58].

The sum of all these terms as given in the penultimate row in Table III is the mass-dependent part of the isotope shift  $\delta\nu_{\text{MS,Theory}}^{6,A}$  between  $^6\text{Li}$  and  $^A\text{Li}$ . It includes the nuclear polarizability correction and the adjusted relativistic recoil term as calculated for the first time in [29]. The difference between this value and the measured isotope shift must arise from the finite nuclear size effect. To extract nuclear charge radii information from this value, the electronic factor  $C_{A,A'}$  as defined in Eq. (2) is required.

The contribution of the finite nuclear size effect to the total transition energy can be written as

$$\Delta E_{\text{nuc}} = C \cdot \bar{r}_c^2, \quad (56)$$

with the mean-square nuclear charge radius  $\bar{r}_c^2 = \langle r_c^2 \rangle$ . The electronic factor  $C$  can be expanded into a power series of  $\alpha$  and  $(\mu/M)$

$$C = \frac{R_\infty m^2 c^3 \alpha^2}{\hbar^2} \times \left( C^{(4,0)} + \frac{\mu}{M} C^{(4,1)} + \alpha^2 C^{(6,0)} + \dots \right), \quad (57)$$

where the  $C^{(m,n)}$  are dimensionless coefficients that refer to corrections on the order of  $\alpha^m(\mu/M)^n$ . The leading-order term is proportional to the nonrelativistic wave function at the origin

$$C^{(4,0)} = \frac{2\pi Z}{3} \Delta |\Psi(0)|^2, \quad (58)$$

and  $C^{(6,0)}$  comes from the relativistic correction to the wave function at the origin [60]

$$C^{(6,0)} \approx -Z^2 \ln(Z\alpha m \bar{r}_c) C^{(4,0)}. \quad (59)$$

Contrary to these terms,  $C^{(4,1)}$  is mass-dependent. It consists of a term originating from the mass scaling and one from the mass polarization [30]. For example, the contributions of these terms to the  $C$ -coefficients of the transition frequency for  $^{6,11}\text{Li}$  are listed in Table IV. As compared with the leading term  $C^{(4,0)}$ , the  $C^{(6,0)}$  and  $C^{(4,1)}$  corrections are of the order  $10^{-3}$  to  $10^{-4}$ . Thus, they are significant in the systematic studies of the isotope shift at the current level of theoretical uncertainties in  $\delta\nu_{\text{MS,Theory}}^{A,A'}$ .

Since the correction term  $C^{(6,0)}$  depends on the nuclear size given by  $\bar{r}_c$ , we have to use initial approximate values  $r_{A0}$  for the charge radii, *e.g.*, those which are obtained in [29]. The influence of this approximation is negligible. With these values we can obtain the  $C_{A,A'}$  coefficient for the isotopes  $A$  and  $A'$  as

$$C_{A,A'} = \frac{r_{A'0}^2 C_{A'} - r_{A0}^2 C_A}{r_{A'0}^2 - r_{A0}^2}. \quad (60)$$



TABLE III: Contributions to the mass shift  $\delta\nu_{\text{MS,Theory}}^{6,A}$  of  ${}^A\text{Li}$  ( $A = 7, 8, 9, 11$ ) relative to  ${}^6\text{Li}$  in the  $2s\ 2S_{1/2} \rightarrow 3s\ 2S_{1/2}$  transition. The mass-dependent terms are calculated using the masses  $M$  listed in the first row. The mass of the reference isotope  ${}^6\text{Li}$  is 6.015122794(16) amu [55]. The nuclear polarizability contribution  $\nu_{\text{pol}}$  is included for  ${}^{11}\text{Li}$  and expected to be negligible for the other isotopes. The unit of the electronic factor  $C_{6,A}$  is MHz/fm<sup>2</sup>. All other values are in MHz. Both sets of theoretical results are given in cases where they differ (see text).

Term	${}^7\text{Li}$	${}^8\text{Li}$	${}^9\text{Li}$	${}^{11}\text{Li}$
$M$ (amu)	7.0160034256(45) <sup>a</sup>	8.02248624(12) <sup>b</sup>	9.02679020(21) <sup>b</sup>	11.04372361(69) <sup>b</sup>
$\mu/M$	11 454.655 2(2) <sup>c</sup>	20 090.837 3(9) <sup>c</sup>	26 788.479 2(13) <sup>c</sup>	36 559.175 4(27) <sup>c</sup>
$(\mu/M)^2$	-1.794 0	-2.964 4	-3.764 2	-4.761 9
$\alpha^2\mu/M$	0.017 2 <sup>d</sup>	0.030 2 <sup>d</sup>	0.040 2 <sup>d</sup>	0.055 0 <sup>d</sup>
	0.016 8(1) <sup>e</sup>	0.029 5(2) <sup>e</sup>	0.039 3(3) <sup>e</sup>	0.053 7(4) <sup>e</sup>
$\alpha^3\mu/M$	-0.048 5(6)	-0.085 1(11)	-0.113 5(15)	-0.154 8(21)
$\alpha^4\mu/M$	-0.009 2(23) <sup>d</sup>	-0.016 1(40) <sup>d</sup>	-0.021 5(63) <sup>d</sup>	-0.029 4(73) <sup>d</sup>
	-0.008 4(28) <sup>e</sup>	-0.014 7(41) <sup>e</sup>	-0.019 6(66) <sup>e</sup>	-0.026 8(90) <sup>e</sup>
$\nu_{\text{pol}}$				0.039(4)
Total	11 452.820 7(24) <sup>d</sup>	20 087.801 9(42) <sup>d</sup>	26 784.620 2(66) <sup>d</sup>	36 554.323(9) <sup>d</sup>
	11 452.821 1(28) <sup>e</sup>	20 087.802 6(50) <sup>e</sup>	26 784.621 3(67) <sup>e</sup>	36 554.325(9) <sup>e</sup>
$C_{6,A}$	-1.571 9(16) <sup>f</sup>	-1.571 9(16) <sup>f</sup>	-1.572 0(16) <sup>f</sup>	-1.570 3(16) <sup>f</sup>

Ref. <sup>a</sup> [56], <sup>b</sup> [53].

<sup>c</sup> Uncertainties for this line are dominated by the nuclear mass uncertainty.

<sup>d</sup> Calculation by Puchalski and Pachucki (this work).

<sup>e</sup> Calculation by Yan and Drake (this work).

<sup>f</sup> A 25% error is assumed for the relativistic correction due to the estimation of the relativistic correction to the wave function at the origin on the basis of a known result for hydrogenic systems.

TABLE IV: Finite size corrections  $C^{(m,n)}$  of the constant  $C$  in MHz/fm<sup>2</sup> for the  $2s \rightarrow 3s$  transition in  ${}^{11}\text{Li}$  and  ${}^6\text{Li}$ .

Coefficient	${}^{11}\text{Li}$	${}^6\text{Li}$
$C^{(4,0)}$	-1.566501	-1.566501
$C^{(6,0)}$	-0.006675	-0.006641
$C^{(4,1)}$	0.000231	0.000424
$C$	-1.572945	-1.572718

The obtained numerical results for constants  $C_{A,A'}$  for the relevant isotope shifts using this relation are included in Table III.

Concerning the accuracy of the calculated mass shift contributions, the uncertainty is largely dominated by the nuclear mass uncertainty for  ${}^{11}\text{Li}$ , as listed in the table. An exception is the relativistic recoil term of order  $\alpha^2\mu/M$ . Because of the almost complete numerical cancellation of individual contributions that were already mentioned, the percentage uncertainty is correspondingly large.

For convenience, the theoretical result relating the measured isotope shift  $\delta\nu$  to the change in the mean-square nuclear charge radii between  ${}^6\text{Li}$  and  ${}^{11}\text{Li}$  is

$$\delta\nu_{2s \rightarrow 3s}^{6,11} = 36\,554.324(9) + 1.570 [\bar{r}_c^2({}^6\text{Li}) - \bar{r}_c^2({}^{11}\text{Li})], \quad (61)$$

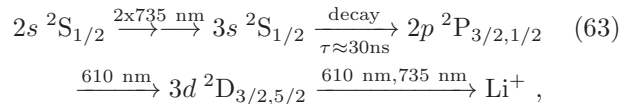
where frequencies are given in MHz and radii in fm. The results presented in Table III are the basis for the extraction of the change in the mean-square charge radius for all lithium isotopes by comparison with the experimental values, according to

$$[\bar{r}_c^2({}^A\text{Li}) - \bar{r}_c^2({}^6\text{Li})] = \frac{\delta\nu_{\text{exp}}^{6,A} - \delta\nu_{\text{MS,Theory}}^{6,A}}{C_{6,A}}. \quad (62)$$

### III. EXPERIMENTAL SETUP

Figure 2 shows an overall schematic of the experimental apparatus used for laser spectroscopy of the  $2s\ 2S_{1/2} \rightarrow 3s\ 2S_{1/2}$  two-photon transition in lithium. Ions of both stable and short-lived lithium isotopes, produced at an accelerator and accelerated to 40 keV, are mass separated and transported to the experimental area. Here they are stopped and neutralized in a thin carbon foil catcher. This foil is heated with a CO<sub>2</sub> laser beam to about 1700-1800 °C, so that the implanted lithium atoms diffuse quickly to the surface. Atoms released in the forward direction drift into the ionization region in front of a quadrupole mass filter (QMF). Here, the lithium atoms are resonantly ionized with laser light at 735 nm and 610 nm according to the three-step four-photon res-

onance ionization scheme



with a two-photon transition followed by spontaneous decay of the  $3s$  state with a lifetime of  $\tau \approx 30$  ns and subsequent resonance ionization as discussed in more detail in Section III C. For brevity, if the meaning is clear, the laser-driven resonance transitions are abbreviated as the  $2s \rightarrow 3s$  and  $2p \rightarrow 3d$  transitions, respectively. The photo-produced ions are then mass analyzed with the QMF and detected with a continuous dynode electron multiplier (CDEM) detector. The isotope shift in the  $2s \rightarrow 3s$  transition is measured by tuning the 735 nm light across the lithium two-photon resonances. The individual parts of the system will be described in detail in the following Sections.

### A. Production of Radioactive Lithium Isotopes

Radioactive lithium isotopes were produced at the on-line mass separator<sup>3</sup> at GSI Darmstadt in 2003 [1] and in

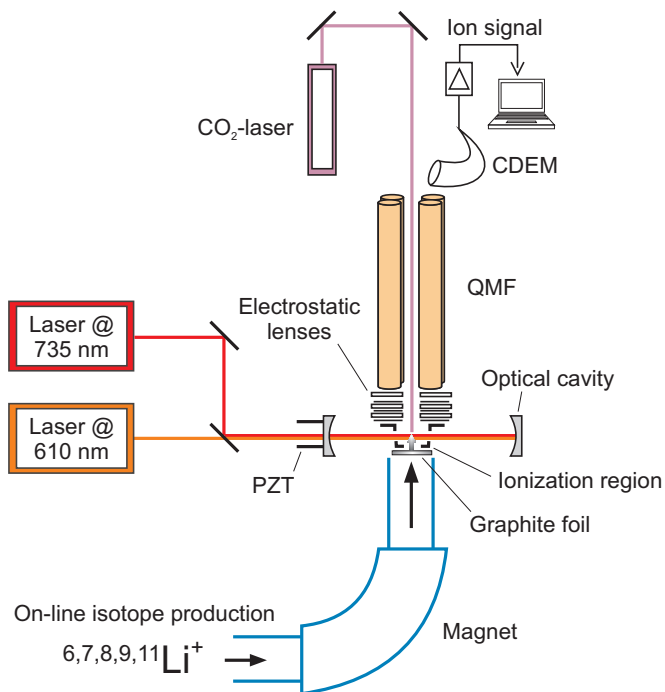


FIG. 2: Experimental setup to measure the  $2s \ ^2S_{1/2} \rightarrow 3s \ ^2S_{1/2}$  electronic transition in lithium. CDEM: Continuous dynode electron multiplier, QMF: Quadrupole mass filter, PZT: Piezoelectric transducer.

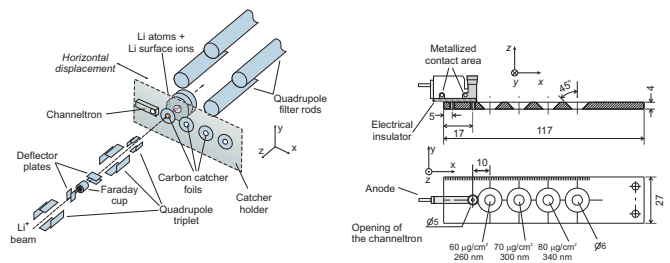


FIG. 3: Schematics of the ion optical setup (left) in front of the catcher holder which holds a channeltron-type continuous dynode multiplier detector for aligning the  $^{11}\text{Li}$  ion beam and several carbon foils of different thickness. Details of the catcher holder are shown on the right. Dimensions are given in mm. The holder, fixed to a linear feedthrough, can be moved in the  $x$ -direction horizontally and vertically in the  $y$ -direction.

TABLE V: Half-lives and typical ion yields in ions/s for the radioactive lithium ions at GSI and ISAC-TRIUMF.

Beamtime	$^8\text{Li}$	$^9\text{Li}$	$^{11}\text{Li}$
Half-life (ms)	838(6)	178.3(4)	8.59(14)
Yield (GSI 2003)	$3.6 \times 10^5$	$1.8 \times 10^5$	-
Yield (TRIUMF 09/2004)	$10^8$	$10^6$	-
Yield (TRIUMF 10/2004)	$8 \times 10^8$	$9 \times 10^7$	$3.5 \times 10^4$

a second experiment at the ISAC mass separator facility at TRIUMF in September and October 2004 [3] (see Table V). The experimental set-ups were almost identical for the two experimental runs. If changes were made, the version used for the TRIUMF experiment is presented in this publication.

At GSI,  $^8,9\text{Li}$  were produced by directing a  $^{12}\text{C}$  beam from the UNILAC with an energy of 11.4 MeV/u onto a 100 mg/cm<sup>2</sup> tungsten target. Fast reaction products entering the hot ion source of the mass separator through a tungsten window were stopped in a sintered graphite catcher. Atoms diffusing out of the catcher were surface-ionized and extracted through a small hole. Ion yields towards the experiment are listed in Table V.

At TRIUMF,  $^8,9,^{11}\text{Li}$  were produced with a 500 MeV primary proton beam of 40  $\mu\text{A}$  extracted from the  $\text{H}^-$  cyclotron. A stack of tantalum foils was used as target in order to allow fast release of the short-lived lithium isotopes that are produced by target fragmentation. The reaction products were surface ionized and extracted from the ion source with a beam energy of 40 keV. Mass separation was obtained with a 60° preseparator magnet followed by a 120° main separator [61]. A fast switch (kicker) installed behind the main mass separator was used to turn the ion beam on and off.

The mass separated ion beam was transported into the ISAC low-energy experimental area, where the ToPLiS experiment was installed. The existing low-energy beam-line was extended to allow installation of deflector plates

<sup>3</sup> The mass separator was shutdown in early 2004.

and a quadrupole doublet, as depicted in Fig. 3, for precise shaping and steering of the ion beam. A similar ion optics was existing at the GSI mass separator. To detect the small number of  $^{11}\text{Li}$  ions delivered to the experiment, a channeltron-type detector was installed on a linear feedthrough that also carries the carbon catcher foils and could be moved into the beam in front of the QMF.

## B. Neutralization and Atomic Beam Generation

After production and mass separation, the 40 keV ion beam had to be converted into a thermal beam of neutral atoms. This process must be efficient and considerably faster than the 8.6 ms half-life of the  $^{11}\text{Li}$  ions. Therefore, the ion beam was directed onto a thin carbon foil (Fig. 3). In this ‘catcher’ foil the ions were stopped and neutralized. “Stopping and Range of Ions in Matter” (SRIM) calculations [62] were used to estimate the thickness of foil that would stop the ions shortly before they reached the back side of the foil. This enabled rapid release of the neutralized atoms in the preferred direction towards the ionization region (Fig. 2). Catcher foils with thickness around 300 nm were prepared in the GSI Target Laboratory and glued onto a stainless steel holder, providing three positions equipped with catcher foils of different thickness (ranging from about 60 to 80  $\mu\text{g}/\text{cm}^2$ ). The target holder was mounted on a linear feedthrough that moves the holder along the  $x$ -position so that foils of different thickness could be located in front of the quadrupole mass filter. The holder was also movable in  $y$  and  $z$  directions to optimize the vertical position of the catcher foil and the distance to the QMF ion optics. As mentioned before, fast release is essential for measurements on  $^{11}\text{Li}$ . In order to achieve this, a 2 mm diameter spot on the catcher foil was heated to about 1800°C with a  $\text{CO}_2$  laser beam that was coupled into the system along the axis of the QMF (see below). As shown in Fig. 4, a release of the implanted atoms within 0.5 ms was observed under these conditions. The temperature of the catcher foil was still sufficiently low that only a very small fraction of about  $10^{-4}$  of the incoming ions were released as surface ions. The release time of the lithium atoms from the graphite catcher foil was measured by observing the increase of surface ions as a function of time after turning the ion beam on. For this purpose the fast kicker at the mass separator was used, the electrostatic ion optics of the QMF were set for surface ion detection and the output of the CDEM detector was fed into a fast timing amplifier for linear pulse amplification. The amplified signal was recorded with a multichannel scaler. The measurement was performed with a beam of stable  $^6\text{Li}$  and the observed signal with a time resolution of 1 ms and 0.05 ms is shown in Fig. 4(a) and 4(b), respectively. The increase in ion beam intensity from a practically background-free baseline is very fast and is not resolved with the time resolution of 1 ms.

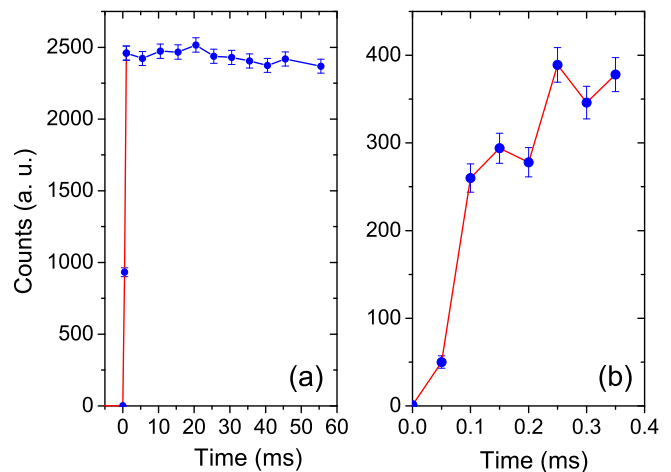


FIG. 4: Time-resolved surface-ion release recorded for  $^6\text{Li}$  to determine the release time at a catcher temperature of about 1700-1800°C. The  $t = 0$  position is approximately the time when the ion beam was turned on. Time resolution was 0.5 ms in (a) but after the first three data points only every tenth channel is shown as an individual data point for clarity. In (b) a resolution of 50  $\mu\text{s}$  was used.

The graph with the higher time resolution (Fig. 4(b)) shows two contributions: The ion signal rises to about 70% of the final level within 100  $\mu\text{s}$  and is then followed by a slightly slower increase to the full intensity which is reached after about 300  $\mu\text{s}$ . A large contribution of ions that have sufficient energy for simply penetrating the foil was never observed. Hence, it is assumed that even the flank was originating from ions that were first stopped in the catcher foil and released again. However, even if the 300  $\mu\text{s}$  time scale would be the relevant one for the release time of neutral atoms, this amounts to only 3% of the  $^{11}\text{Li}$  half-life and is clearly sufficient to have a good release efficiency. The total conversion efficiency of the foils was estimated to be about 50 % and the transport efficiency into the laser beam to 20%.

## C. Excitation and Ionization Scheme

The laser excitation and ionization scheme has to provide both, high resolution and high efficiency in order to detect the signal for ion yields of only a few thousand ions/s with an accuracy of about 0.1 MHz.

Figure 5 shows the level scheme for neutral lithium with the excitation path chosen for resonance ionization: Lithium atoms in the  $2s\ ^2S_{1/2}$  ground level are excited via the Doppler-free two-photon transition at 735 nm to the  $3s\ ^2S_{1/2}$  level. This transition offers a narrow resonance and leads to efficient excitation since all velocity classes can be excited simultaneously. However, relatively large intensities are required for saturation. The two-photon excitation is followed by a spontaneous decay into the  $2p\ ^2P_J$  levels. Atoms in the  $2p\ ^2P_J$  levels are subse-

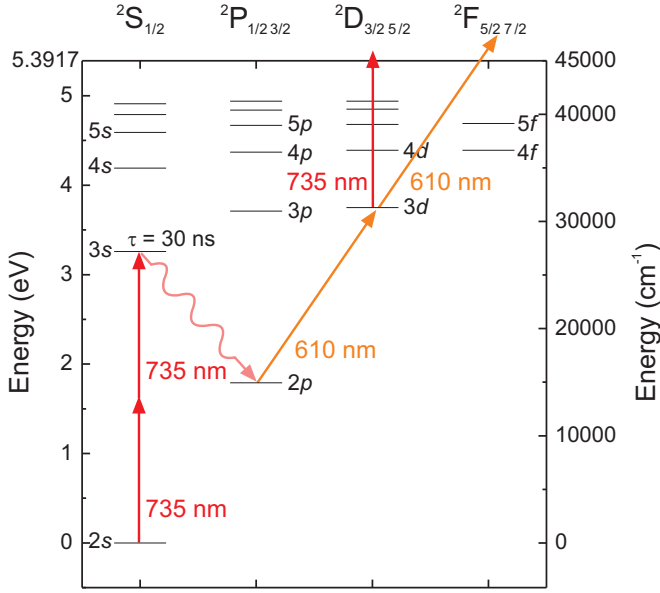


FIG. 5: Resonance ionization scheme for lithium as used in the reported experiments.

quently excited into the  $3d\ ^2D_J$  levels with resonant laser light at 610 nm and then photoionized by absorption of a photon at either 735 nm or 610 nm. In this way the states used for measuring the isotope shift are decoupled from the states used for ionization and detection which results in a strong reduction of the AC-Stark broadening and AC-Stark shifts [63]. Compared with fluorescence detection, this multi-step excitation and ionization followed by mass-selective ion detection has the advantage that the  $2s \rightarrow 3s$  resonance can be detected with a very high efficiency and an extremely high signal-to-background ratio.

#### D. Mass Spectrometer

To achieve the additional background suppression, mass selective ion detection is used. Quadrupole mass filters (QMF) provide ideal conditions to mass separate the ions with thermal energies that are produced in the laser ionization process described above [64, 65].

Therefore, the laser beams have to be overlapped with the thermal atom cloud in a region from which the created ions can be extracted into the QMF. Moreover, surface ions that are produced on the hot catcher foil must be efficiently suppressed, because every surface ion of the isotope under investigation entering the laser beam cannot be distinguished from a photo ion and will produce background events.

The QMF used for the reported experiment was a commercial instrument from ABB Extrel (ABB Extrel, Pittsburgh, USA, Model No. 150 QC) with 9.39 mm radius rods of 21 cm length and a free-field radius of  $r_0 = 8.33$  mm. The system is driven at a frequency

of 2.9 MHz and can be used for ions up to  $A/q \leq 64$ . This model provides transmission close to 100 % and an excellent neighboring mass suppression as has been demonstrated in simulations [65, 66], ultratrace analysis applications [67, 68], and measurements discussed below. Ions transmitted through the QMF were detected with an off-axis continuous dynode electron multiplier (CDEM) detector. The entrance opening of the channeltron was biased with about -2000 V such that the positive ions were accelerated in the CDEM.

For the measurements reported here, the ionization region of the QMF was modified as shown in Fig. 6. The original axial electron impact ion source of the EXTREL device was removed and the electrodes before the quadrupole structure were replaced by specifically designed electrodes allowing free access for the laser beams. The distance between the catcher foil and the ionization region was 2 - 3 mm to have an efficient transfer of the released atoms into the ionization region. The QMF ion optics could be operated to accept either laser-created ions from inside the ion region or surface ions created on the hot carbon catcher foil. In the first mode, the ion region (Fig. 6) was held at 3.9 V relative to the grounded catcher foil. This repels catcher surface ions, while neutral atoms can enter the laser ionization region. The potential difference between the catcher foil and the ionization region was small enough to ensure that electrons emitted from the hot catcher surface and accelerated into the ion region, do not gain sufficient energy to ionize lithium atoms by electron impact ionization (Li ionization potential: 5.39 eV). Photo ions were then extracted by the negative extractor voltage and focussed into the QMF rod structure using the remaining electrostatic lenses. In the second mode, surface ions produced at the hot catcher foil were accelerated into the QMF with a negative voltage at the ion region and the extractor was operated as another lens for adapting the beam properties to the QMS acceptance. Ion optical settings of all lenses for both detection modes are summarized in Table VI. Ions transmitted through the rod system were focussed with an exit lens and detected with the CDEM detector model DeTech 5402AH-021, which was chosen

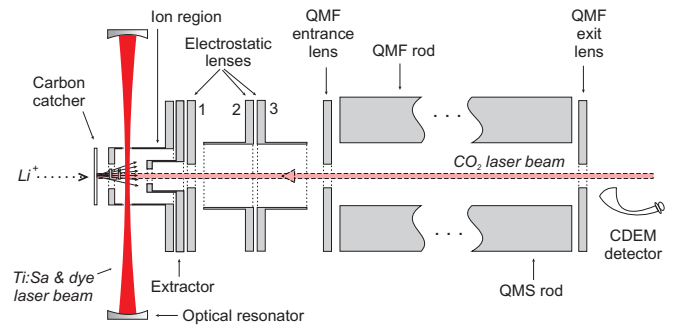


FIG. 6: Schematics of the optical resonator, the ion optics, the quadrupole mass filter (QMF) and the continuous dynode electron multiplier (CDEM) detector.

TABLE VI: Settings for the extractor, the electrostatic lenses and the quadrupole mass filter (see Fig. 6) for the detection of either surface ions or photo ions produced by resonance ionization. All values are in V. Pole bias is an additional common DC voltage that is applied to all four QMF rods to change the kinetic energy of the ions entering the rod system.

	Ion Region	Extractor	Lens 1	Lens 2	Lens 3	Entrance Lens	pole bias	exit lens
Laser Ions	+3.9	-9	-43	+8	-43	+2	0	-2
Surface Ions	-4.9	-165	-60	-310	-60	-7	-1.4	+9

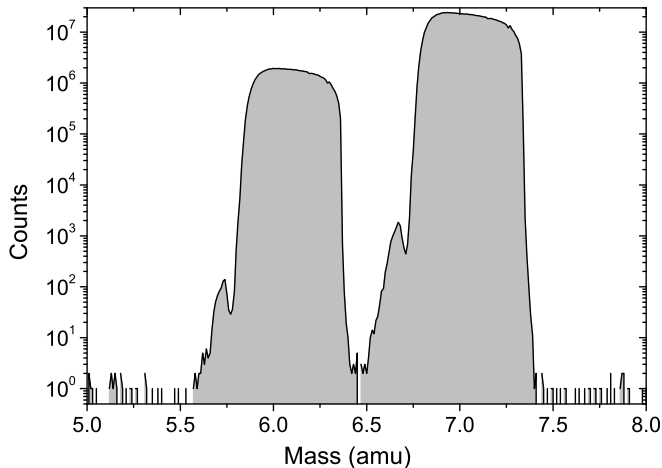


FIG. 7: Mass spectra of the stable lithium isotopes  ${}^6\text{Li}$  and  ${}^7\text{Li}$ .

for its very low dark count rate of typically 5 to 20 mHz.

The lithium isotopes were produced with rates that differ by orders of magnitude (see Table V). For additional suppression of neighboring isotopes, the QMF was tested with ions on the stable isotopes  ${}^6,{}^7\text{Li}$  produced by surface ionization on the hot carbon catcher foil. Ion optical parameters of the QMF extraction and transport optics were optimized in order to obtain a flat top profile with steep flanks and maximum transmission. An example for the peak profile of surface ions is shown in Fig. 7. Typically, a suppression of neighboring masses of  $> 10^8$  was achieved. The dark count rate of the CDEM detector was about 10 mHz.

The entire QMF system consisting of ion source, quadrupole mass filter and ion counting was computer controlled using the commercial Extrel Merlin data acquisition and control electronics. The system was installed in a vacuum chamber and pumped by a turbomolecular pump, which provided residual gas pressures in the range of  $10^{-7}$  mbar, even when the graphite catcher was heated.

### E. Laser System and Enhancement Cavity

The excitation and ionization scheme discussed in Section III C requires laser systems that provide the high power required to saturate the two-photon transition and

to efficiently drive the ionization steps and at the same time a sufficiently small bandwidth, high stability and precise frequency control to reach the required accuracy for the isotope shift measurements.

For the two-photon transition it is important to have two exactly counterpropagating laser beams in the laser ionization region. It is also favourable to have these beams well balanced in power to avoid an asymmetry in the background signal due to Doppler-broadened two-photon excitation as discussed below. The laser system that fulfilled all these requirements was composed of two argon ion laser pumped ring lasers, a titanium:sapphire (Ti:Sa) laser and a dye laser, combined with a Fabry-Perot cavity around the laser interaction region to enforce the counterpropagating beams and the high intensities that are required for the two-photon transition. Because both laser beams must interact with the atoms simultaneously, this solution required a cavity that is kept in resonance with the two laser beams having strongly different wavelengths. High-accuracy frequency determinations were achieved by referencing the Ti:Sa laser to an iodine-stabilized diode laser.

#### 1. Iodine-Locked Reference Laser

A stable reference frequency for the isotope shift measurement was realized by an amplified diode laser system locked to a hyperfine component in the molecular spectra of  ${}^{127}\text{I}_2$ . To obtain a detectable beat frequency between the Ti:Sa laser and the reference diode laser while the Ti:Sa laser frequency was tuned across the  $2s \rightarrow 3s$  transition in lithium, the iodine transition had to be within approximately 50 GHz of the two-photon resonance frequency. Hence, the  $X^1\Sigma_g^+ \rightarrow BO_u^+ R(114) 11-2$  transition in iodine was chosen. The  $a_1$  hyperfine component has a predicted resonance frequency of 407 815 138 (30) MHz according to the ‘iodine spec 4’ program [69]. Recent measurements accurately determined the frequency as 407 815 137.15 (30) MHz [70]. This is very close to the lithium two-photon transitions with the isotopes  ${}^6,{}^7,{}^8\text{Li}$  having resonance frequencies below and  ${}^9,{}^{11}\text{Li}$  above the iodine transition frequency. The largest separation is for  ${}^6\text{Li}$  and is approximately 11.5 GHz. Stabilization of the diode laser to the iodine transition was achieved using frequency modulation (FM) saturation spectroscopy [71], with the experimental arrangement shown in Fig. 8. The light produced by

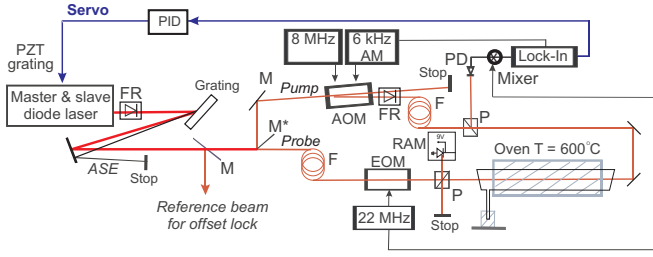


FIG. 8: Diode laser system locked to an iodine line for frequency reference. ASE: Amplified spontaneous emission, AOM: Acousto-optical modulator, EOM: Electro-optical modulator, F: Fiber, FR: Faraday rotator, M: Mirror, P: Polarizer, PD: Photodiode, PID: Proportional-integral-differential regulator, PZT: Piezoelectric transducer for tuning the grating of the master laser, RAM: Residual amplitude modulation.

the master laser (Toptica, Model PDL 100) was amplified in a broad-area diode laser (BAL 740-100-1, Sacher) and separated from the weak amplified spontaneous emission (ASE) of the amplifier with a diffraction grating. The spatially-extended amplified beam was split at the edge of a mirror into a pump and a probe beam with intensity ratio of about 2:1. The pump beam was frequency-shifted (8 MHz) and amplitude-modulated (AM) at 6.6 kHz with an acousto-optical modulator (AOM) and then sent through a single-mode fiber (Newport S-FS-C) to obtain a good TEM<sub>00</sub> mode structure. The probe beam was first sent through a mode-cleaning fiber and then frequency-modulated (22 MHz) with an electro-optical modulator (EOM) for side-band generation. The signal in FM saturation spectroscopy after simultaneous interaction of the counterpropagating probe and pump beam with the iodine vapour is carried by the amount of amplitude modulation of the probe beam at the EOM frequency. Hence, residual amplitude modulation (RAM) of the phase-modulated probe beam introduced by a non-ideal matching of the laser beam polarization to the EOM would have caused an offset signal in the detection that shifts the locking point away from the resonance center. Therefore the RAM was actively suppressed by separating a small part of the laser beam after the EOM and detecting intensity fluctuations at the EOM frequency on a fast photodiode. A feedback loop that regulated a high-voltage DC offset on the EOM was used to remove the spurious RAM as described in [72].

The probe and pump beams were superimposed in a counterpropagating geometry with perpendicular polarization in an iodine vapor cell (pump beam: 5 mW, probe beam: 3 mW, beam diameters 1 mm). The beams were combined and separated with Rochon polarizers. After passage through the iodine cell and separation from the pump beam, the probe beam was directed onto a photodiode. The photodiode signal was amplified and demodulated with a mixer at the 22 MHz EOM frequency. The mixer intermediate frequency (IF) output was then fed into a lock-in amplifier for phase-sensitive detection

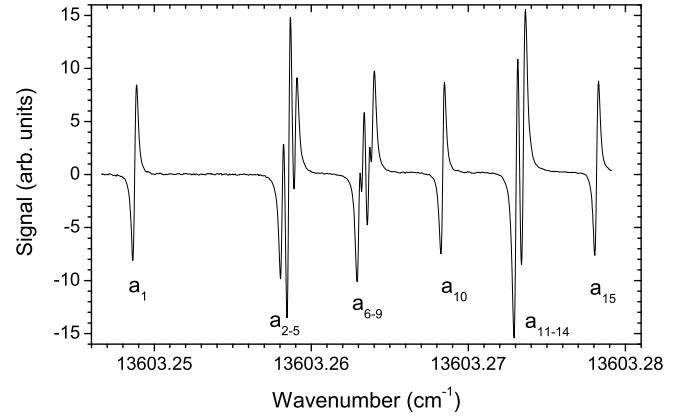


FIG. 9: Hyperfine structure spectrum of the  $X^1\Sigma_g^+ \rightarrow BO_u^+$  R(114) 11-2 reference iodine line measured with the set-up shown in Fig. 8.

to extract the signal at the 6.6 kHz frequency that was applied to the AOM driver to amplitude-modulate the pump beam.

A typical spectrum of the iodine transition obtained by scanning the unlocked diode laser across the hyperfine resonances is shown in Fig. 9. To lock the laser to one of the isolated hyperfine components, it was coarsely tuned to the frequency of the I<sub>2</sub> a<sub>1</sub> transition guided by a wavemeter. The output of the lock-in amplifier was used as input signal for a PID regulator to produce a servo signal for the diode laser stabilization. The a<sub>1</sub> hyperfine component of the transition was chosen as the reference transition since it is clearly separated from the other hyperfine components and could be easily identified to facilitate reliable relocking during the measurements.

To populate sufficiently the  $\nu = 11$  vibrational level of the I<sub>2</sub> electronic ground state, the iodine cell is heated in an oven to 600°C. The iodine reservoir is kept outside the oven in a cold finger at a fixed temperature of 29°C to control the vapor pressure inside the cell. Pressure broadening of the lines was only observed at cold-finger temperatures well above 30°C, the pressure-dependent shift of a few kHz/Pa [70] is not relevant for the accuracies targeted in the measurements reported here.

## 2. The Titanium:Sapphire Laser

The 735 nm light for the lithium  $2s \rightarrow 3s$  two-photon transition was produced by a Coherent 899-21 titanium sapphire (Ti:Sa) ring laser pumped with 15 W from an argon ion laser (multi-line visible). The Ti:Sa laser provided up to 1 W of single-frequency output with a typical linewidth of approximately 1 MHz. Short-term frequency fluctuations were suppressed by locking the laser to the external Fabry-Perot cavity that is part of the Coherent 899-21. Medium ( $\geq 30$  ms) and long-term stabilization was achieved with a frequency-offset lock of the Ti:Sa laser relative to the iodine stabilized diode laser. About

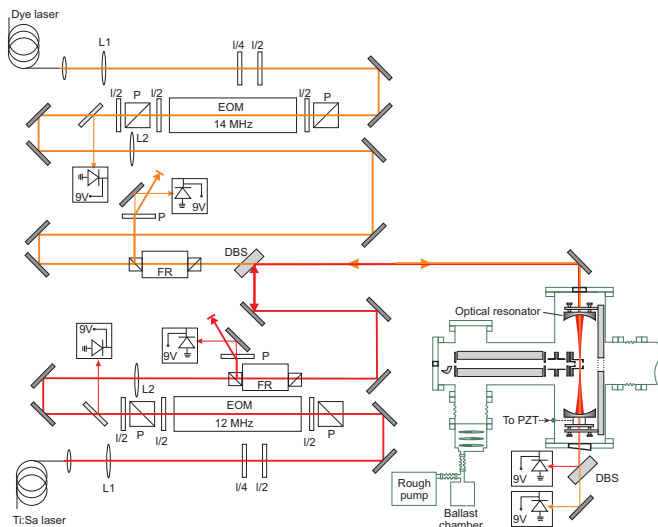


FIG. 10: Optical setup of the Pound-Drever-Hall stabilisation of the dye laser (coming from top) and the Ti:Sa laser (coming from the bottom) and injection of the laser beams into the experimental setup for resonance ionization spectroscopy of lithium isotopes. DBS: Dichroic beamsplitter mirrors, EOM: Electro-optical modulators for side-band generation, FR: Faraday rotators for separation of the reflected laser beams and detection with fast photodiodes, L: Mode-matching lenses,  $\lambda/4$  and  $\lambda/2$ : Waveplates for polarisation adaption, P: Polarizers, PZT: Piezoelectric transducer.

1 mW of light from the reference diode laser was superimposed with a few mW from the Ti:Sa laser by coupling each into the two arms of a fiber-optical beamsplitter. One of the output arms with the mixed laser beams was connected to the fiber-optical input of a fast photodiode (New Focus, Model 1434, 25 GHz), while the output of the second arm was collimated and mode matched into a 300 MHz Fabry-Perot interferometer for spectral analysis of the diode and the Ti:Sa laser beams. The radio frequency (RF) output signal of the fast photodiode, *i.e.*, the beat signal between the Ti:Sa laser and the diode laser, was amplified with an ultra-wideband amplifier (MITEQ Model JS4-001020000-30-5A) and then divided with a two-way splitter. One part was guided to a microwave frequency counter (Hewlett Packard, Model 5350B), while the second part was used for frequency offset locking of the Ti:Sa laser. To obtain the respective servo signal, the beat frequency was mixed with the RF output of a synthesized sweeper (Hewlett Packard, Model 83752A) and a frequency difference of exactly 160 MHz between the sweeper and the beat frequency was maintained. This was accomplished with a frequency discriminator (MiTeq, Model FD-2PZ-160/10PC) that provided an output voltage proportional to the deviation of the input frequency from 160 MHz. Its output was fed into a PID regulator and the correction signal applied to the external scan input of the Coherent Ti:Sa laser. The bandwidth of the feedback loop was approximately 30 Hz. By changing the frequency of the synthesized sweeper,

the Ti:Sa laser could be set and stabilized to any arbitrary frequency around the iodine reference line within the bandwidth of the fast photodiode ( $\pm 25$  GHz). An upper limit for the laser linewidth could be obtained from the frequency spectrum of the beat signal. At GSI it was usually on the order of 1 MHz [1], while at TRIUMF a slightly larger linewidth of 2 to 3 MHz was observed. This increase was mainly due to the frequency jitter of the diode laser, caused by the acoustic noise of a CAMAC crate located nearby. However, with about 1 s integration time, the average frequency measured by the frequency counter was stable to within a few 10 kHz.

The Ti:Sa laser light was transported from the laser laboratory to the experimental hall with a 25 meter long photonic-crystal fiber (Crystal Fibers, LMA-020) that can transmit high cw powers without significant losses and without indication of nonlinear Brillouin scattering due to its large mode area [73]. Typical transmission through the fiber was about 80% for 1 W input Ti:Sa laser power.

### 3. Light Enhancement Cavity

High intensities are required to approach saturation for the  $2s \rightarrow 3s$  two-photon transition and hence efficient detection. One approach that is often used in Doppler-free two-photon spectroscopy is strong focussing of two counterpropagating laser beams to reach saturation intensity. However, this has the disadvantage of poor spatial overlap between the two laser beams and the atomic beam released from the graphite catcher. Hence, we developed an optical enhancement cavity to both ensure collinearity of the counterpropagating beams and to obtain higher intensities. A critical point is that both laser beams, one for the two-photon resonant excitation and the other for the  $2p \rightarrow 3d$  excitation, *i.e.*, the Ti:Sa and the dye laser beams, must be coupled to the cavity simultaneously. In designing this cavity one has also to consider that the spatial profile of the resonator mode should provide a relatively large focus to ensure sufficient spatial overlap with the atomic beam.

Figure 10 shows the cavity together with the optical setup for stabilization. The symmetrical cavity has a length of approximately 30 cm and mirror curvature radius of 50 cm. The diameter of the TEM<sub>00</sub> mode in the focus is therefore relatively large and is approximately 500  $\mu\text{m}$ . The cavity is placed completely inside the vacuum chamber with two mirror holders mounted on a vertically oriented baseplate. The input coupling mirror above the ionization region of the QMF has a transmittance of 98% while the high reflector mounted below has reflectivities of  $R > 99.93\%$  for both wavelengths (735 nm, 610 nm). The high reflector is fixed to a piezoelectric transducer (PZT) for fine tuning of the cavity length.

The cavity length is actively stabilized to the Ti:Sa laser frequency using Pound-Drever-Hall locking [74, 75].

Collimating optics for the fiber, lenses for spatial mode-matching and sideband generation with an EOM required for the locking scheme is mounted on a breadboard on top of the vacuum chamber. The Ti:Sa light is first focused through an EOM operated at 12 MHz. Similar to the diode laser modulation discussed in Section III E 1, an active feedback loop suppresses residual amplitude modulation. After passing through an initial polarizer and Faraday rotator, the main Ti:Sa beam is superimposed on the dye laser beam (see below) using a dichroic beamsplitter that is highly reflective for 735 nm at 45° incidence and antireflection coated for 610 nm. Behind the dichroic beamsplitter, a broadband mirror directs the combined laser beams vertically through an antireflection-coated viewport into the vacuum chamber and to the enhancement cavity. Light reflected by the input coupler of the cavity is separated at the input polarizer after returning through the Faraday rotator and detected with a fast Si-PIN photodiode. Depending on the resonance condition of the cavity, the two sidebands created by the EOM modulation exhibit different phase shifts and a dispersionlike signal is obtained after demodulation of the photodiode signal at the EOM frequency. This signal is used to generate a PID-regulated servo signal (0-500 V), which is applied to the PZT to change the cavity length. This stabilizes the cavity length to the Ti:Sa frequency and tracks it while tuning across the resonance transitions of the different lithium isotopes. The effective tuning range of the cavity for PZT voltage variations of 500 V is about 600 MHz and thus sufficient to cover the hyperfine structure of each lithium isotope (typically 300 MHz) without relocking the servo loop.

Such an optical resonator is extremely sensitive to vibration because the distance of the mirror positions must be stabilized within a small fraction of the laser wavelength, *i.e.* less than 10 nm. To decouple the vacuum chamber with the optical cavity from vibrations caused by vacuum pumps and other mechanical devices, the two cross pieces housing the experiment (Fig. 10) are connected to the beam line only through a flexible metal bellow, while the roughing pump is isolated from the chamber turbo pump by flexible tube couplings to and from a massive ballast chamber mounted on the floor.

Fluctuating light intensity inside the cavity has a strong influence on the observed lineshape for two reasons: The quadratic dependence of the excitation efficiency increases the sensitivity of the signal intensity to vibrationally induced power changes. Even more important, changing intensities cause fluctuating AC-Stark shifts of the transition frequencies. These are discussed in more detail below. Therefore it is important to monitor the light power contained within the resonant cavity. To do so, the light transmitted through the high reflector, which is about 0.05% and 0.07% of the power inside the cavity for 735 nm and 610 nm, respectively, leaves the vacuum chamber through a second viewport. A second dichroic beamsplitter separates the two wavelengths and send them to two photodiodes where their intensity

is recorded. From this averaged signal a power enhancement of about 80 to 100 was determined for the cavity.

#### 4. Dye Laser

Laser light at 610 nm is required to drive the  $2p\ ^2P_J \rightarrow 3d\ ^2D_{J'}$  transitions in lithium. This was produced by a Coherent 699-21 dye laser operated with a Rhodamine 6G solution in ethylene glycol and pumped with 6 W of multiline visible output of a second argon ion laser. The laser light was transported from the laser laboratory to the experimental hall with a second large-mode-area photonic-crystal fiber (LMA-020). In this case, transmission efficiencies up to about 70% for 600 mW input dye laser power were achieved. This light had also to be resonantly coupled into the optical cavity together with the Ti:Sa laser light. Hence, the dye laser was locked to a longitudinal cavity mode that was as close as possible to the  $2p\ ^2P \rightarrow 3d\ ^2D$  transition frequency. This was achieved using a second Pound-Drever-Hall servo loop depicted in Fig. 10, but the servo signal was applied to the external-scan input of the Coherent 699 dye laser controller (rather than to the PZT controlling the length of the enhancement cavity). This approach does not allow tuning the dye laser exactly to the  $2p \rightarrow 3d$  resonance transitions, but the high laser intensities caused strong power broadening of the allowed dipole transition, as will be discussed in the next Section. With typical power broadened linewidths of 7 GHz (FWHM) and a free spectral range of the optical cavity of 500 MHz it was always possible to find a locking point that provided maximum excitation efficiency and kept the dye laser frequency in a region of constant excitation efficiency.

#### F. Data Acquisition

Data acquisition (DAQ) of the experiment was based on the Multi-Branch System (MBS) developed at GSI. A CAMAC-GPIB controller allowed communication with the RF synthesizer and the microwave counter. Digital-to-analog, analog-to-digital converters and scalars were directly implemented in the CAMAC crate. The MBS system worked stand-alone. It read all data from a CAMAC crate and wrote it on a local tape drive. No other computers were necessary to take data and to store them. For analysis, the data of each scan was transferred via a TCP/IP connection into the data analysis package Origin 7.0, running on a PC. Routines written with C++ in the Origin environment were finally used to analyze the data. Nonlinear least-square fits of lineshapes were performed with a Levenberg-Marquardt algorithm adapted from Numerical Recipes [76].



## IV. RESULTS AND DISCUSSION

We present and summarize results and data from the preparatory experimental phase at GSI and TRIUMF and the four beamtimes that were performed at these facilities: an on-line beamtime at GSI in December 2003, an off-line beamtime at TRIUMF in June 2004, and two on-line beamtimes at TRIUMF in September and October 2004.

### A. Lineshapes

Determination of the isotope shift on the level of 100 kHz or better requires a detailed understanding and description of the resonance lineshape and all factors affecting it. Hence, this Section starts with an analysis of the observed lineshapes and the influence of the AC-Stark effect in the  $2s\ ^2S_{1/2} \rightarrow 3s\ ^2S_{1/2}$  as well as in the  $2p\ ^2P_J \rightarrow 3d\ ^2D_{J'}$  transitions. Afterwards, the measurements of the hyperfine structure (HFS) and isotope shift (IS) of the stable and short-lived isotopes are discussed.

#### 1. $2s \rightarrow 3s$ Two-Photon Transition

Resonance profiles of the  $2s \rightarrow 3s$  transition were recorded in the following way: First, the Ti:Sa laser was tuned to a frequency below the  $2s \rightarrow 3s$  resonance of the respective isotope and frequency-offset locked to the iodine-stabilized diode laser. Then, the enhancement cavity was locked to the Ti:Sa laser and finally the dye laser was locked to the longitudinal mode of the cavity closest to the  $2p \rightarrow 3d$  transition frequency of the respective isotope. The Ti:Sa laser was scanned by slowly varying the RF frequency for the frequency-offset lock in steps of 1 MHz. Maximum scan ranges were about 600 MHz, limited by the voltage range of the high-voltage power supply for the piezoelectric transducer (PZT) at the enhancement cavity. Since the HFS of all lithium isotopes in the two-photon transition is smaller than this scanning range the complete resonance structure can be covered with a single scan.

Figure 11 shows an overall resonance profile obtained for  $^7\text{Li}$ . The observed count rate at the channeltron-type detector is plotted as a function of the measured beat frequency between the iodine-locked diode laser and the Ti:Sa laser. Here, a large tuning range was used to record also the far-reaching wings of the resonance profile. Therefore the complete scanning range of about 2 GHz was divided into scans of approximately 400 MHz range in order to stay inside the tuning range of the cavity PZT and to limit the frequency variation of the dye laser (see below). After each 400 MHz scan, the cavity and the dye lasers were relocked to keep the dye laser frequency as close to the  $2p \rightarrow 3d$  resonance frequency as possible.

The profile exhibits two narrow Doppler-free components that are labeled with their  $F$  quantum numbers.

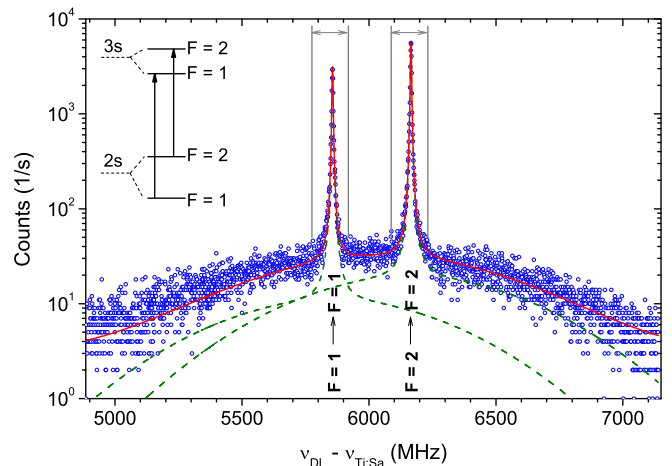


FIG. 11: Wide-range line profile of the  $^7\text{Li}$   $2s \rightarrow 3s$  two-photon transition with narrow Doppler-free hyperfine transitions and the Doppler-broadened background as observed off-line at GSI. On the  $x$ -axis, the beat frequency between the iodine-stabilized diode laser and the Ti:Sa laser is given. The solid (red) line is a fit of two Voigt profiles including a wide Doppler background pedestal. The dashed (green) line shows the individual contributions of the two hyperfine components. The regions marked by vertical lines are the scanning regions in  $^7\text{Li}$  on-line experiments. The inset shows schematically the hyperfine splitting in the  $2s$  and  $3s$  states of the  $I = 3/2$  isotopes  $^7,9,11\text{Li}$  and the allowed ( $\Delta F = 0$ ) two-photon transitions.

According to the selection rules for a two-photon transition between  $s$  states, only hyperfine transitions with  $\Delta F = 0$  are allowed. The wide Doppler-broadened background with a relative amplitude of about 1% of the peak intensity and a Gaussian width of approximately 1.7 GHz is caused by the absorption of two photons from copropagating beams [77]. To account for this process, each of the two peaks is fitted by applying a Levenberg-Marquardt minimization procedure with a Voigt plus a background Gaussian function represented by the dashed (green) lines. Both HFS components are constrained to have identical width parameters for the Voigt as well as the Gaussian lineshape of the background. The Voigt profile shows a Lorentzian linewidth  $\Gamma_L$  of 4.5 MHz which is already slightly larger than the natural linewidth of 2.6 MHz, attributed to saturation broadening, and a Gaussian linewidth  $\Gamma_G$  of 1 MHz, fitting well to the observed laser linewidth. Here, all width parameters refer to the Ti:Sa laser frequency scale and have to be doubled to obtain the value for the  $2s \rightarrow 3s$  two-photon transition. The solid (red) line is the overall fitting function which shows an excellent agreement with the experimental data points over more than 2 GHz frequency range and about three orders of magnitude in signal intensity.

For precise frequency determination, only the regions around the two Doppler-free peaks are important and scans of the radioactive isotopes were thus usually performed by scanning about  $\pm 30$  or  $\pm 15$  MHz around the

resonance centers, as indicated in Fig. 11, skipping the intermediate part in fast steps without data taking. Such spectra of  ${}^6\text{Li}$  and  ${}^7\text{Li}$ , taken at the GSI on-line mass separator and the Off-Line Isotope Separator (OLIS) at TRIUMF, respectively, are depicted in Fig. 12. The incoming ion yield was about  $3 \cdot 10^5$  ions/s for  ${}^6\text{Li}$  and  $2 \cdot 10^8$  ions/s for  ${}^7\text{Li}$ , while approximately 80 and  $10^5$  ions/s were obtained in resonance on the strongest hyperfine transition. This corresponds to overall efficiencies of  $\approx 2 \cdot 10^{-4}$  at GSI and  $5 \cdot 10^{-4}$  at TRIUMF. The observed efficiencies agree quite well with those calculated and estimated during the design of the setup as listed in Table VII.

Before fitting the recorded spectra, the observed number of ion events ( $N_{\text{Raw}}$ ) was normalized for each channel with the Ti:Sa laser power ( $P_{\text{Ti:Sa}}$ ) that was recorded with the photodiode located behind the enhancement cavity (see Fig. 10) while the atoms were irradiated with the constant laser frequency:

$$N_{\text{Norm}} = N_{\text{Raw}} \cdot \left( \frac{P_{\text{Ti:Sa}}}{\langle P_{\text{Ti:Sa}} \rangle} \right)^{-2}. \quad (64)$$

Here  $\langle P_{\text{Ti:Sa}} \rangle$  is the average Ti:Sa laser power while recording the complete spectrum. The uncertainty of  $N_{\text{Norm}}$  was calculated from the statistical uncertainty and from the laser power fluctuations using Gaussian error propagation. To confirm the normalization function, a  $\chi^2$  optimization was performed using different normalization exponents and checking for the lowest  $\chi^2$  value in the subsequent lineshape fitting. The optimum was found to scatter between 1.7 and 2.8, and hence the theoretically expected factor of 2 seems to be well justified.

The red fit curves are Voigt profiles including a Doppler background with a width fixed to 1.7 GHz as obtained from Fig. 11. The Lorentzian and Gaussian linewidths of the narrow Voigt profile as well as the relative intensity of the Doppler background are constrained to be equal for both hyperfine structure components. The width of the Gaussian pedestal was varied within a reasonable range ( $\approx 1 - 3$  GHz) and does not show considerable influence on the fitted peak centers. The fitting curves of the individual peaks are indicated by the green dashed lines. This procedure was used for all isotopes.

In the lower part of Fig. 12, the residuals of the fit are plotted. A slight systematic asymmetry is visible in the  ${}^7\text{Li}$  spectrum while it is much less pronounced in the residuals of the  ${}^6\text{Li}$  resonance fit. In later experiments performed off-line at GSI, a much stronger and clearly visible asymmetry of the peaks was observed which is discussed in detail in a recent publication [27]. There it is shown that the asymmetry is caused by the Gaussian profile of the laser beam. Atoms passing through the laser beam in the interaction region experience an intensity-dependent AC-Stark shift as will be discussed in the next section. Therefore, the exact atomic resonance frequency depends on the position within the laser beam where the excitation and ionization occur. This line profile distortion is similar for all isotopes under identical

experimental conditions. Therefore, the line shape calculations described in [27] show that the influence of this asymmetry on the extracted isotope shift is very small. However, its contribution is significant if the total transition frequency is to be extracted. Then a total correction by about 160 kHz is required [27].

To calculate the isotope shift, the resonance positions of the individual hyperfine components obtained from the fit must be converted into center-of-gravity (cg) frequencies. Since the nuclear quadrupole moment does not affect the  $J = 1/2$  states in the transition, only the magnetic hyperfine interaction must be considered. The energy shift of the hyperfine state with angular momentum  $F$  relative to the  $J$ -level energy is in first order given by

$$E_{\text{HFS}} = \frac{A}{2} C_F = \frac{A}{2} [F(F+1) - J(J+1) - I(I+1)] \quad (65)$$

with the Casimir factor  $C_F$  and the magnetic dipole hyperfine constant  $A$ . In first-order perturbation theory, the hyperfine structure cg coincides with the unperturbed  $J$ -level energy and can be calculated from the two hyperfine resonances in the  $2s \rightarrow 3s$  transition of lithium according to

$$\nu_{\text{cg}} = \frac{C_F \nu_{F'} - C_{F'} \nu_F}{C_F - C_{F'}}, \quad (66)$$

where  $\nu_F$  is the transition frequency of the  $F \rightarrow F$  transition. For  ${}^{7,9,11}\text{Li}$  with nuclear spin  $I = 3/2$ , this leads for example to  $\nu_{\text{cg}} = \frac{5}{8}\nu_2 + \frac{3}{8}\nu_1$ .

Figure 13 shows the Lorentzian linewidth of the two-photon transition as a function of the Ti:Sa laser intensity inside the cavity  $\langle I_{\text{Ti:Sa}} \rangle$ . The intensity was calculated from the power transmitted through the high reflector of the enhancement cavity with a measured cavity mirror transmission of 0.05(1)% and a calculated cavity mode diameter of 0.46 mm. The solid red line is a fit of the function for the power-broadened linewidth of a two-photon transition

$$\Gamma_L = \Gamma_0 \sqrt{1 + (\langle I_{\text{Ti:Sa}} \rangle / I_{\text{Sat}})^2} \quad (67)$$

to the data points, where  $\Gamma_0 = 3.08(2)$  MHz is the extrapolated natural linewidth for vanishing intensity of the Ti:Sa laser and  $I_{\text{Sat}} = 148(2)$  W/mm<sup>2</sup> is the saturation intensity. These results are in good agreement with values obtained in a previous beamtime at GSI, where  $\Gamma_0 = 3.2(1)$  MHz and  $I_{\text{Sat}} = 167(6)$  W/mm<sup>2</sup> were obtained. The uncertainty of the absolute value of  $I_{\text{Sat}}$  is solely the fitting uncertainty and includes neither the uncertainty in the mirror transmission and the transmission through the entrance window<sup>4</sup> nor the uncertainty of the effective diameter of the laser focus. Hence an additional

<sup>4</sup> The window transmission shows an etalon effect discussed below and changes slightly as a function of the laser wavelength.

TABLE VII: Estimated partial efficiencies and expected overall efficiency for the detection of lithium ions compared with that experimentally observed.

Release efficiency of the catcher foil	50 %
Overlap between laser beams and atomic beam (diam. 0.5 mm)	20 %
Excitation efficiency for the $2s \rightarrow 3s$ two-photon transition	25 %
Ionization efficiency via $2p \rightarrow 3d \rightarrow$ continuum	3 %
Signal reduction by HFS splitting	62 %
Transmission of the quadrupole mass filter	90 %
Quantum efficiency of the detector	80 %
Expected overall efficiency on resonance	$2.5 \cdot 10^{-4}$
Experimental overall efficiency at GSI	$2 \cdot 10^{-4}$
Experimental overall efficiency at TRIUMF	$5 \cdot 10^{-4}$

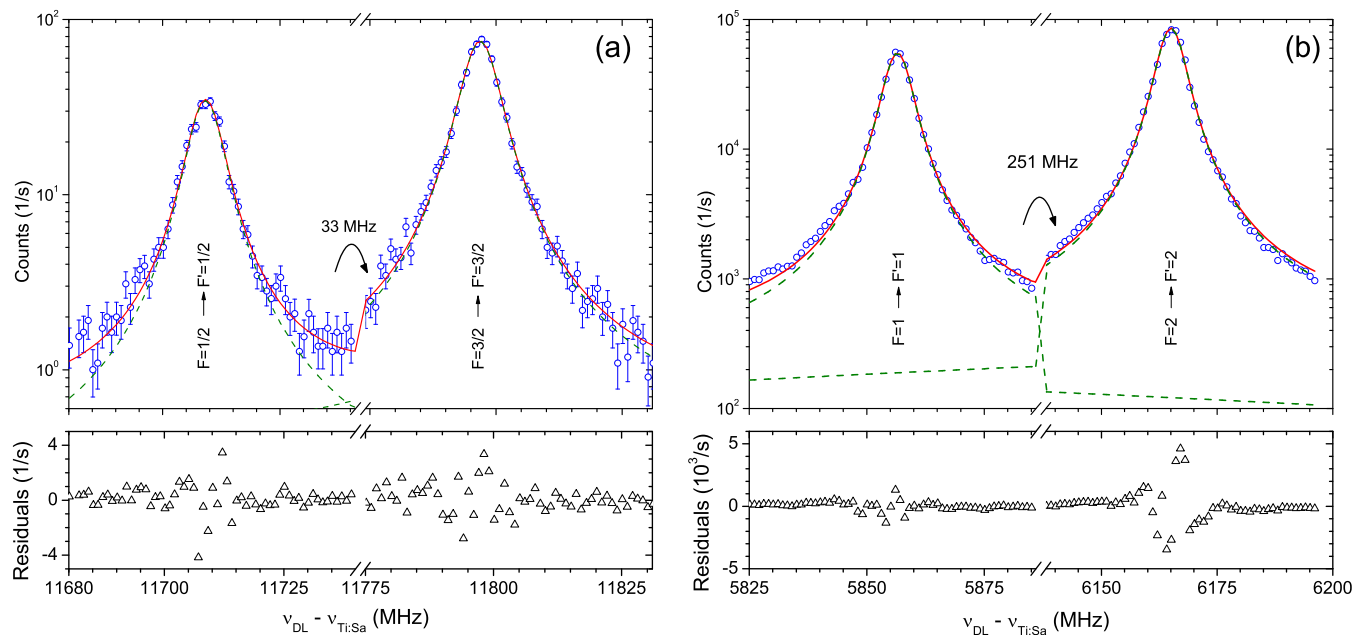


FIG. 12:  $2s \rightarrow 3s$  two-photon resonances for (a)  ${}^6\text{Li}$  obtained at GSI and for (b)  ${}^7\text{Li}$  recorded at TRIUMF. The  $x$ -axis break indicates the intermediate region that was skipped. The solid (red) line is the common fit function while the dashed (green) lines are the contributions of the individual hyperfine components. The residuals (differences between the experimental points and the common fit function) are plotted at the bottom.

uncertainty of about 20% should be added if these values are to be compared with calculations or other measurements. The small deviation of the fit value  $\Gamma_0$  from the natural linewidth  $\Gamma_{0\text{nat}} = 2.65$  MHz is either caused by laser intensity fluctuations inside the cavity, resulting in varying AC-Stark shifts for the atoms of the ensemble, or an artefact from the fit program.

## 2. $2p \rightarrow 3d$ Resonance

The lineshape of the two-photon transition is distorted if the ionization efficiency along the  $2p \rightarrow 3d \rightarrow \text{Li}^+$  ionization path changes during the scan. This could happen because the change in the Ti:Sa laser frequency during a

scan of the  $2s \rightarrow 3s$  transition induces also a change of the dye laser frequency. This cannot be avoided since the dye laser is locked to the enhancement cavity and the resonator length must be changed when scanning the Ti:Sa laser frequency. Hence, the dye laser frequency is changed typically by a few hundred MHz during the scan. Helpful is here the strong power broadening of the  $2p \rightarrow 3d$  transition. The high intensity of the 610 nm light in the cavity focus considerably broadens the linewidth of the  $2p \rightarrow 3d$  transition. This broadening was studied to find maximum excitation efficiency and to ensure a constant ionization efficiency along the whole scan. The results for different laser powers as they were available at TRIUMF and GSI are shown in Fig. 14. The main reason for the different power levels is the fiber transport from the laser

laboratory to the experimental hall. While a 50 m long standard single-mode fiber was used for the dye laser at GSI, a large mode area (LMA) photonic crystal fiber was applied at TRIUMF with a transport distance of 25 m. Hence 20 mW of dye laser light were coupled to the enhancement cavity at GSI while 80 mW were available at TRIUMF.

The resonance profiles in Fig. 14 were obtained in the following way: First the QMF was set to detect photoions of the respective isotope and the Ti:Sa laser frequency was fixed at the resonance of the strongest hyperfine transition and operated at about 25% of the maximum achievable power. Then, the frequency of the dye laser was set to a value clearly below resonance and changed manually until a longitudinal mode of the enhancement cavity was reached. There, the dye laser frequency was locked to the cavity and resonant laser ions were detected for a period of 3 s before the dye laser was taken out of lock and its frequency changed until the next longitudinal cavity mode was reached. The free spectral range of the cavity was approximately 500 MHz which determined the step size. The intensity of the incoming  $\text{Li}^+$  ion beam as well as of the Ti:Sa laser was sufficiently constant during the measurements and a normalization of the count rate therefore not required.

In Fig. 14 the detected ion count rates (circles) are plotted as functions of the dye laser frequency that was determined with a Fizeau-type wavemeter. The solid line is a fit of two Lorentzian profiles with equal widths to the data and serves only to guide the eye. The profile (a) obtained at GSI with lower dye laser power shows a flat-top region with an extension of about 1.5 GHz. That is sufficient to ensure constant ionization efficiency since the scan width of the Ti:Sa laser was less than 500 MHz for all isotopes. In (b), recorded with the higher dye laser power that was available at TRIUMF, the flat re-

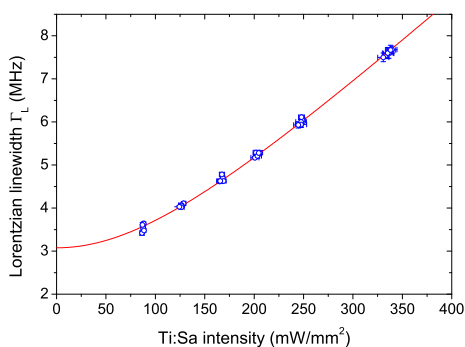


FIG. 13: Lorentzian linewidth of  $^6\text{Li}$  resonances as a function of the Ti:Sa laser intensity as obtained in off-line experiments at TRIUMF. The solid line is a fit by  $\Gamma_L = \Gamma_0 \sqrt{1 + (I/I_{\text{Sat}})^2}$ , describing the saturation for a two-photon transition. The Ti:Sa laser intensity is calculated based on the laser power behind the high reflector of the enhancement cavity as described in the text. Please note that the linewidth refers to the Ti:Sa laser frequency and must be doubled for the full  $2s \rightarrow 3s$  transition.

gion extends to approximately  $0.1 \text{ cm}^{-1}$  (3 GHz) width, ideal for looking the dye laser during a scan. The region of the first resonance agrees roughly with the reported transition frequencies of  $16\,379.0661 \text{ cm}^{-1}$  and  $16\,379.1021 \text{ cm}^{-1}$  [78] for the  $2p\ ^2P_{3/2} \rightarrow 3d\ ^2D_{3/2}$  and  $2p\ ^2P_{3/2} \rightarrow 3d\ ^2D_{5/2}$  resonances in  $^7\text{Li}$ , respectively. Obviously, the dye laser power at TRIUMF was sufficient to even excite the tails of the  $2p\ ^2P_{1/2} \rightarrow 3d\ ^2D_{3/2}$  transition at  $16\,379.4014 \text{ cm}^{-1}$  [78]. Contrary, in the measurements at GSI (Fig. 14(a)), where less dye laser power was available, the  $2p\ ^2P_{1/2} \rightarrow 3d\ ^2D_{3/2}$  transition is still clearly resolved. Thus, we can expect the overall efficiency at TRIUMF to be about 30% larger than that obtained at GSI since the dye laser will also excite and ionize the fraction of atoms decaying from the  $3s\ ^2S_{1/2}$  to the  $2p\ ^2P_{1/2}$  state. This is in accordance with the higher efficiencies obtained at TRIUMF as reported above.

The frequency of the  $2p\ ^2P_{3/2} \rightarrow 3d\ ^2D_{5/2}$  resonances for the unstable isotopes were calculated from the isotope shift formula

$$\delta\nu^{AA'} = K_{\text{MS}} \cdot \frac{M_A M_{A'}}{M_A - M_{A'}}, \quad (68)$$

with  $K_{\text{MS}} = 117.812 \text{ GHz}\cdot\text{amu}$  being the mass shift coefficient obtained from the known  $^6,^7\text{Li}$  isotope shift data [78] and neglecting all field shift contributions. The calculated resonance frequencies that were used for setting the dye laser frequency are listed in Table VIII.

## B. AC-Stark Shift

Since atoms experience relatively strong fields when crossing the laser beam focus in the resonator, the atomic level energies will be altered by AC-Stark shifts. To correct for these shifts, spectra were recorded at different light powers. To distinguish between the effects caused by the Ti:Sa and the dye laser light, the power of one of the lasers was varied while keeping the other laser intensity constant during the measurements. The observed cg frequencies were plotted against the power level of the respective laser detected on the photodiodes behind the cavity high-reflector. These values were not converted into intensities at the laser focus since this conversion includes a large uncertainty due to the mirror and window transmission functions and the effective laser diameter inside the focus. Figure 15(a) shows the  $^6\text{Li}$  cg frequency as a function of the Ti:Sa (a) and the dye laser power (b). In both cases a linear relation is observed as is expected for an off-resonance AC-Stark shift. Hence, the linear function

$$\nu_{\text{cg}} = b_0 + b_1 \langle P \rangle \quad (69)$$

is fitted to the data points from which the slopes

$$b_1^{\text{Ti:Sa}} = -0.0549(14) \text{ MHz/mW} \quad \text{and} \quad (70)$$

$$b_1^{\text{Dye}} = 0.115(14) \text{ MHz/mW} \quad (71)$$

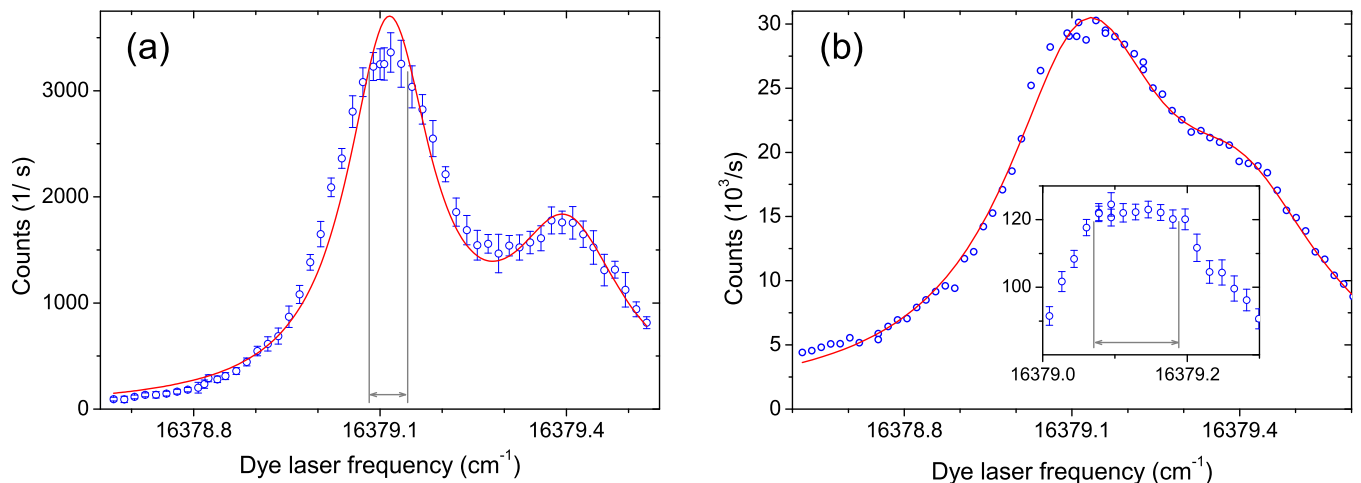


FIG. 14: Strongly saturated resonance profiles of the  $2p \rightarrow 3d$  transition in  ${}^7\text{Li}$  as obtained with 20 mW laser power entering the resonator at GSI (a) and with 80 mW at TRIUMF (b). Frequencies were measured with a Fizeau-type interferometer and have uncertainties of about  $3 \cdot 10^{-3} \text{ cm}^{-1}$ . Circles indicate the experimentally obtained signal and the solid line is a fit of two Lorentzian line profiles with identical widths to the data. This curve is only to guide the eye since the strong saturation and the unresolved  ${}^2\text{D}_{3/2,5/2}$  levels lead to a distorted line shape. The flat-top regions used for spectroscopy in the  $2s \rightarrow 3s$  transition are indicated by vertical lines. The inset in (b) is the result of another scan with higher statistics around the flat-top region.

TABLE VIII: Mass shift  $\delta\nu_{2p-3d,\text{MS}}^{6,A}$  and resonance frequencies  $\nu_{2p-3d}$  of the  $2p {}^2\text{P}_{3/2} \rightarrow 3d {}^2\text{D}_{5/2}$  transition in lithium isotopes based on the  ${}^6,{}^7\text{Li}$  transition frequencies reported in [78].

Isotope	${}^6\text{Li}$	${}^7\text{Li}$	${}^8\text{Li}$	${}^9\text{Li}$	${}^{11}\text{Li}$
$\delta\nu_{2p-3d,\text{MS}}^{6,A}$ (MHz)	0	2794	4901	6535	8918
$\nu_{2p-3d}$ ( $\text{cm}^{-1}$ )	16379.0089	16379.1021	16379.1724	16379.2269	16379.3064

are obtained. In both fits of Fig. 15, the 95% confidence bands are indicated. The dye and the Ti:Sa laser intensities influence the level energies in opposite directions, resulting in the different signs of the slope. Even though the sensitivity on the dye laser intensity is stronger, the absolute shift that it causes is much smaller due to the relatively low power levels compared with the Ti:Sa laser. Varying from highest to lowest applied power, the Ti:Sa laser light shifts the  $2s \rightarrow 3s$  frequency by about 1.5 MHz, the dye laser light only by 150 kHz. Hence, it was concluded that it is sufficient to keep the dye laser power as constant as possible during all measurements whereas such power series measurements were performed with the Ti:Sa laser for all isotopes excluding  ${}^{11}\text{Li}$ . For the latter isotope the production rates were not high enough to produce sufficient statistics at low laser power. A remaining small influence of the AC-Stark shift, caused by power variations of the dye laser while taking the Ti:Sa laser power-series, was included in the uncertainty of the isotope shifts as discussed below.

### C. Hyperfine Structure and Isotope Shifts

A large number of measurements on the stable isotopes was performed during the preparation of the experiments and the four beamtimes that were performed at GSI and TRIUMF. Spectra like those shown in Fig. 12 were analyzed by fitting the lineshapes as discussed above and determining the center of gravity frequency  $\nu_{\text{cg}}$  and the hyperfine splitting  $\Delta\nu_A^{\text{HFS}}$  from the peak positions. Spectra of the radioactive isotopes will be presented in the following Sections.

#### 1. Hyperfine Structure

The hyperfine structure splitting in an atomic transition is determined in first-order perturbation theory by the following nuclear ground state properties: spin  $I$ , magnetic moment  $\mu$ , and the spectroscopic electric quadrupole moment  $Q_s$ . Values of those are listed for all lithium isotopes in Table IX. Additionally, the magnetic hyperfine constant  $A_{2s}$  in the  $2s {}^2\text{S}_{1/2}$  electronic ground state, which is directly proportional to the magnetic moment, is included in the table. For the stable isotopes they are well known from atomic beam magnetic reso-

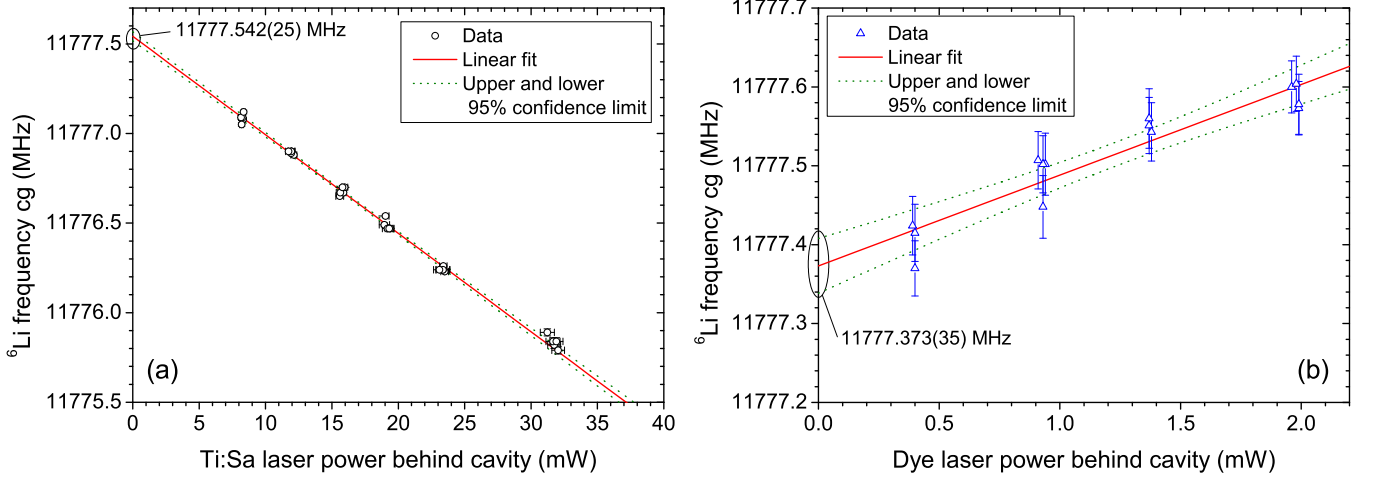


FIG. 15: AC-Stark shift in the  $2s \rightarrow 3s$  transition of  ${}^6\text{Li}$  caused by (a) the Ti:Sa laser light at 735 nm and (b) the dye laser light at 610 nm. In (a) the power of the dye laser was fixed to 50 mW in front of the cavity and in (b) the power of the Ti:Sa laser was fixed to 330 mW during the measurements. The solid lines are linear regression lines while the dashed lines indicate the 95% confidence bands of the fit.

TABLE IX: Nuclear spins and parity  $I^\pi$ , experimental dipole  $\mu_I$  and spectroscopic quadrupole moments  $Q_s$  of the investigated lithium isotopes from [21, 22].  $A_{2s}$  values are taken from [79] for the stable isotopes and are calculated based on the ratio of the magnetic moments for the short-lived ones.

Property	${}^6\text{Li}$	${}^7\text{Li}$	${}^8\text{Li}$	${}^9\text{Li}$	${}^{11}\text{Li}$
$I^\pi$	$1^+$	$3/2^-$	$2^+$	$3/2^-$	$3/2^-$
$\mu_I$ ( $\mu_N$ )	0.8220473(6)	3.2564268(17)	1.653560(18)	3.43678(6)	3.6712(3)
$Q_s$ (mb)	-0.806(6)	-40.0(3)	+31.4(2)	-30.6(2)	(-)33.3(5)
$A_{2s}$ (MHz)	152.136840(3)	401.752044(3)	153.017(3)	424.031(7)	452.954(37)

nance measurements [79] and for the short-lived isotopes they are calculated based on the ratio of the magnetic moments taken from [21, 22].

The spectra of the two-photon transitions recorded here, provides only information about the hyperfine splitting  $\Delta\nu^{\text{HFS}}$  between the  $F = I + 1/2 \rightarrow F = I + 1/2$  and the  $F = I - 1/2 \rightarrow F = I - 1/2$  transitions. Separate determinations of the hyperfine splitting in the ground and the excited state are therefore not possible. However, using the information listed in Table IX, the hyperfine splitting in the excited  $3s \ ^2S_{1/2}$  level can be extracted according to

$$A_{3s}({}^A\text{Li}) = A_{2s}({}^A\text{Li}) - \frac{\Delta\nu_A^{\text{HFS}}}{I + J}. \quad (72)$$

and the results will be used to check for an indication of hyperfine anomaly which might be expected for such an extended nucleus like  ${}^{11}\text{Li}$ .

Results for  $\Delta\nu^{\text{HFS}}$  are plotted in Fig. 16. Here, each data point is the average of typically 10 to 20 measurements with the standard error of the mean (SEM) as statistical uncertainty. The rightmost data point is the overall weighted average, where the standard deviation of all results is represented with the dashed lines and

used as the final uncertainty. Additionally,  $\chi^2$ -fitting of a constant to the data points was performed. It resulted in reduced- $\chi^2$  values between 0.5 and 2.0 for all isotopes, indicating that the SEM of such a set of measurements is a realistic estimation of the corresponding statistical uncertainty. Hence, for  ${}^{11}\text{Li}$ , for which in total 24 spectra were obtained (see below), the corresponding SEM is used as uncertainty of the weighted average of all individual measurements. The average values and uncertainties obtained in this way are listed in the first line of Table X.

The  $A$  factors of the  $3s$  state were calculated using Eq. (72) and are listed in the last line of Table X. The current result for  $A_{3s}({}^7\text{Li})$  disagrees with the previous experimental determination by Stark spectroscopy [80], but is in excellent agreement with a previous laser spectroscopic measurement on an atomic beam [25] and with theoretical values, obtained by both Hylleraas variational [81] and multiconfiguration Hartree-Fock methods [82]. Also, the ratio  $A_{3s}({}^7\text{Li})/A_{3s}({}^6\text{Li}) = 2.6407(10)$  is in good agreement with the  $2s$  ground state ratio of 2.6407282(1) from Ref. [83], indicating no hyperfine anomaly at the level of precision available in these experiments. The  $A_{3s}$  factor of the short-lived isotopes  ${}^8,{}^9\text{Li}$  as obtained from

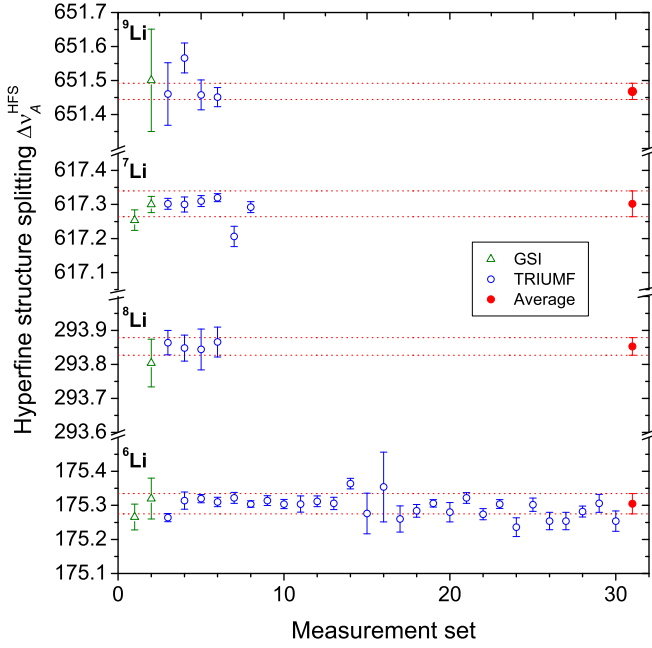


FIG. 16: Results of all hyperfine splitting measurements in the  $2s\ ^2S_{1/2} \rightarrow 3s\ ^2S_{1/2}$  transition of Li isotopes as obtained during the off-line and on-line beamtimes at GSI and TRIUMF. Plotted are the measured two-photon frequency intervals  $\Delta\nu_A^{\text{HFS}}$  (twice the Ti:Sa laser frequency difference) between  $F \rightarrow F$  transitions for  $F = I - 1/2$  and  $F = I + 1/2$ . Each data point (circle) is the average of 10-20 measurements. The rightmost data point represents the weighted average. For their uncertainties see caption of Table X.

our measurements are also listed.

According to [81], the magnetic dipole coupling constant in a  $^2S_{1/2}$  state can be written as

$$A_{1/2}(\text{exp}) = 95.410\ 67(7) \frac{g_e \mu_I f_{\text{exp}}}{3I} \quad (73)$$

in MHz. The experimental Fermi contact term  $f_{\text{exp}}$  can now be extracted from the known magnetic hyperfine constant  $A_{2s}$ . According to theory  $f_{\text{exp}}$  is connected to the uncorrected Fermi contact term  $f_c$  by the factorization:

$$f_{\text{exp}} = \frac{2(1+a_e)}{g_e} C_{\text{rel}} C_M C_R C_{\text{QED}} f_c. \quad (74)$$

Here,  $f_c$  is the fermi contact term as obtained from non-relativistic Hylleraas variational calculations for a point dipole,  $a_e$  denotes the anomaly of the electron magnetic moment,  $C_{\text{rel}}$  is a relativistic correction factor,  $C_M$  the finite mass correction,  $C_R$  the finite size correction and  $C_{\text{QED}}$  are QED corrections other than the  $a_e$ . The finite size effect originates from the nuclear moment distribution in the nucleus and cannot be evaluated independently of a nuclear model. For a one-electron ion, the correction is given by the Zemach correction

$$C_R = 1 - 2Z\langle R_{\text{em}} \rangle / a_0 \quad (75)$$

with the Bohr radius  $a_0$  and the average electromagnetic charge radius  $\langle R_{\text{em}} \rangle$  for the nucleus obtained by folding the charge and magnetization distributions with sizes  $R_c$  and  $R_m$ , respectively. The result for  $\langle R_{\text{em}} \rangle$  depends somewhat on the model chosen for the distributions. To calculate the size of possible effects, two models are applied that are discussed also in [81]. In both cases it is assumed that  $R_c = R_m$  and either an exponential distribution  $e^{-\Lambda r}$  or a Gaussian distribution is used. This results in different prefactors and therefore different values for  $\langle R_{\text{em}} \rangle$

$$\langle R_{\text{em}} \rangle_{\text{exp}} = \frac{35}{16\sqrt{3}} R_c \quad \text{and} \quad \langle R_{\text{em}} \rangle_{\text{Gauss}} = \frac{4}{\sqrt{3\pi}} R_c. \quad (76)$$

The charge radii obtained from our measurement and discussed in the next Chapter as well as the magnetic moments from literature (Table IX) allows us to calculate the Zemach contributions [81] for all isotopes and the hyperfine splitting  $\Delta\nu_{\text{Theo}}^{\text{HFS}}(2s \rightarrow 3s)$ . The results are included in Table X. The influence of the two models is small and no model can be favored within the accuracy of our results. Even in the case of the halo nucleus  $^{11}\text{Li}$  where the assumption  $R_c = R_m$  is for sure not fulfilled, the values for the theoretical and experimental HFS splittings lie almost all in the range of the  $1\sigma$  uncertainties.

## 2. Isotope Shift of $^{6,7}\text{Li}$

The isotope shift  $\delta\nu_{\text{IS}}^{6,7}$  between the two stable isotopes was extracted from measurements of the dependence of  $\delta\nu_{\text{IS}}$  on the Ti:Sa laser power and by calculating the AC-Stark shift regression lines for both isotopes as discussed above. A typical result is shown in Fig. 17. Note that the  $y$ -axis frequency scale in the AC-Stark shift plots is always given in terms of the Ti:Sa laser frequency. Hence, the isotope shift in the  $2s \rightarrow 3s$  two-photon transition is twice the distance between the  $y$ -axis intercepts of the two AC-Stark shift regression lines, as indicated in the figure. At this point, the laser power is zero and the atomic level energies are unperturbed by the laser light. For both regression lines the 95% ( $2\sigma$ ) confidence interval (CFI) was also calculated and is plotted in the graph (dashed lines). The statistical uncertainty ( $1\sigma$ ) of the extracted isotope shift was determined from the fitting result ( $1\sigma$  confidence limit) and an additional uncertainty of 10 kHz was added to account for dye laser power fluctuations during the measurements of the Ti:Sa-induced AC-Stark shift. This value was obtained using the  $b_1^{\text{Dye}}$  coefficient according to Eq. (71) and assuming dye laser power fluctuations up to 1/3 of the total power as a conservative estimate. Such fluctuations might tilt the AC-Stark shift line systematically in a single set. However, they will fluctuate statistically between different sets and the further statistical treatment is expected to be justified.

Results of all isotope shift measurements performed at GSI and at TRIUMF are summarized in Table XI and

TABLE X:  $2s \rightarrow 3s$  hyperfine splitting  $\Delta\nu^{\text{HFS}}$  (twice the difference in Ti:Sa laser resonance frequencies between the  $F = I + 1/2 \rightarrow F = I + 1/2$  and the  $F = I - 1/2 \rightarrow F = I - 1/2$  transitions) of the lithium isotopes and calculated  $A_{3s}$  constants according to Eq. (72). The  $A_{2s}$  constants listed in Table IX are used. Uncertainties of the average are the geometric sum of the statistical uncertainty and a 10 kHz systematic contribution caused by a possible unresolved Zeeman effect in the stray magnetic field at the beamline as discussed in Section IV D. Theoretical values  $\Delta\nu_{\text{Theo}}^{\text{HFS}}$  for the hyperfine splitting are obtained from a calculation of the Fermi contact term [81] and experimental nuclear magnetic moments. They include a finite nuclear size (Zemach) correction with exponential ( $e^{-\Lambda r}$ ) and Gaussian (Gauss) electromagnetic distributions [81] as discussed in the text.

	${}^6\text{Li}$	${}^7\text{Li}$	${}^8\text{Li}$	${}^9\text{Li}$	${}^{11}\text{Li}$
$\Delta\nu_{\text{Exp}}^{\text{HFS}}$ (Average)	175.305(23)	617.302(22)	293.853(34)	651.468(29)	696.09(10)
$\Delta\nu_{\text{Exp}}^{\text{HFS}}$ (PNNL) [25]	175.311(24)	617.291(22)	-	-	-
$\Delta\nu_{\text{Theo}}^{\text{HFS}}$ ( $R_c \propto e^{-\Lambda r}$ )	175.295(17)	617.264(60)	293.851(29)	651.470(65)	695.88(9)
$\Delta\nu_{\text{Theo}}^{\text{HFS}}$ ( $R_c \propto \text{Gauss}$ )	175.305(17)	617.289(60)	293.867(23)	651.502(64)	695.92(9)
$A_{3s}$	35.267(15)	93.101(11)	35.476(14)	98.297(16)	104.91(6)

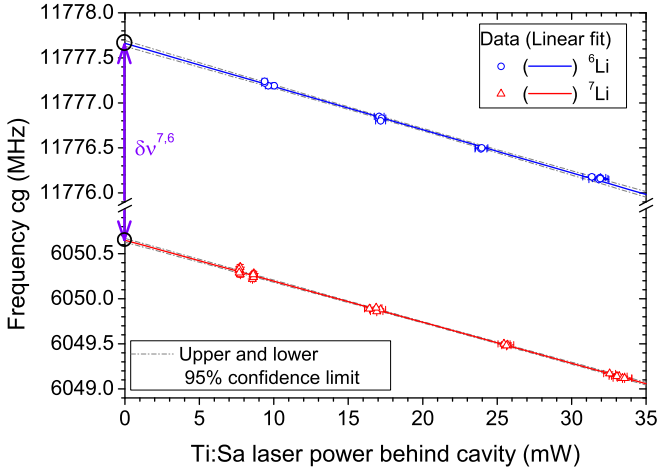


FIG. 17: Determination of the  $\delta\nu_{\text{IS}}^{6,7}$  isotope shift from the AC-Stark shift measurement. The frequency offset  $|\nu_{\text{TiSa}} - \nu_{\text{DL}}|$  between the Ti:Sa and the iodine-locked diode laser at the center-of-gravities of the  ${}^6\text{Li}$  (upper line) and  ${}^7\text{Li}$  (lower line) hyperfine structures is plotted as a function of the Ti:Sa laser power. The  $x$ -axis is the average Ti:Sa laser power observed on a photodiode behind the enhancement cavity while recording the resonance. This power is proportional to the light intensity at the waist of the resonator mode where the atoms cross the laser beams. It is varied between the maximum obtainable value and 25% of the maximum value. The dye laser power was kept constant at the maximum obtainable power during all measurements. A linear shift of the resonance positions is observed which is caused by the AC-Stark shift effect. The solid lines are linear fits to the data points and the dashed lines indicate the 95% confidence bands. The isotope shift  $\delta\nu^{6,7}$  in this two-photon transition was calculated by taking twice the distance between the intercepts with the  $y$ -axis as indicated by the arrow.

plotted in Fig. 18. Each entry corresponds to an extrapolation from an AC-Stark shift measurement as it is shown in Fig. 17. The isotope shifts obtained in the individual sets at TRIUMF were averaged, weighted with the uncertainty, and the weighted error is taken as the fi-

nal statistical uncertainty. Fitting a constant to the data points, as shown in Fig. 18 (bottom graph for  ${}^6,7\text{Li}$ ), results in a reduced- $\chi^2$  between 0.5 and 1 for all isotopes. This  $\chi_{\text{red}}^2$  was not used to scale the final uncertainty. Excellent agreement between the TRIUMF average and the previous measurements at GSI is found for the  ${}^6,7\text{Li}$  isotope shift. The combined values from all ToPLIS experiments, including those at GSI, are listed in the table and marked “Average”.

Since the dye laser power fluctuates statistically, its influence on the line position was added to the statistical uncertainty. Other effects may contribute with systematic shifts in a preferred direction. The estimated size of these systematic uncertainties is given in the caption of Table XI. It includes contributions from the small line-shape asymmetry mentioned before (10 kHz) and possible contributions from unresolved Zeeman shifts caused by stray magnetic fields (10 Hz) which will be discussed in Section IV D.

The isotope-dependent velocities cause a differential second-order Doppler shift (SODS) between the isotopes  ${}^6\text{Li}$  and  ${}^A\text{Li}$  with mean-square velocities  $\langle v_6^2 \rangle$  and  $\langle v_A^2 \rangle$  according to

$$\delta\nu_{\text{SODS}}^{6,A} = -\frac{\nu_0}{2} \frac{\langle v_A^2 \rangle - \langle v_6^2 \rangle}{c^2}. \quad (77)$$

Here, we used the value  $\langle v_A^2 \rangle = 3/2 \cdot 2k_B T/M_A$  for the most probable velocity of the atoms in the “quasi”-collimated atomic beam that enters the laser focus. A catcher temperature of  $T \approx 2000$  K is estimated and  $\nu_0 = 815.61$  THz is the  $2s \rightarrow 3s$  transition frequency ( $2 \cdot \nu_{\text{TiSa}}$ ) [27]. Due to the uncertainty of the absolute temperature and the insufficient knowledge of the exact velocity distribution, an uncertainty of about 30% is assumed for this correction. Absolute shifts are on the order of 30-60 kHz and the differential values are included in Table XI. The largest effect appears naturally for the pair  ${}^6\text{Li}$  -  ${}^{11}\text{Li}$ , which amounts to  $\delta\nu_{\text{SODS}}^{6,11} = 34(11)$  kHz.

The values reported here were carefully reanalyzed with respect to statistical and systematic uncertainties



including effects that were discovered and evaluated [27] after the original publication [3]. Hence, the values and uncertainties do slightly deviate from those given in our earlier work. However, these changes are small and do not significantly alter the determination of nuclear charge radii and their final uncertainty. Note also that all isotope shifts listed in Table XI are given relative to  ${}^6\text{Li}$ , whereas they were earlier given relative to  ${}^7\text{Li}$ . The reason for this is twofold: First, the data in Table XI are the direct results since we have used  ${}^6\text{Li}$  as the reference isotope during the measurements. Second, as will be described in a following publication, a reevaluated nuclear charge radius of  ${}^6\text{Li}$  appears to be more reliable than the previously used reference radius of  ${}^7\text{Li}$ .

The final value of the ToPLiS measurements for the  ${}^{6,7}\text{Li}$  isotope shift agrees with the result obtained at GSI [1, 2] but differs from a previously reported one [25] by about four times the combined uncertainties as listed in the last line of Table XI. This is attributed to unaccounted systematic errors in the prior interferometric measurements. The data reported here are based on beat frequency determinations. Possible sources of systematic errors are nonlinearities in the scan of the confocal Fabry-Perot interferometer (FPI) or changes in the effective length of the interferometer with pointing and wavelength. The latter might be caused, for example, by a wavelength dependent phase change of the multilayer dielectric mirrors of the FPI. Moreover, the FPI was calibrated at the reference lines of Rb at 778 nm and Cs at 851 nm, while the operational wavelength for the measurement was relatively far away at 735 nm for lithium.

### 3. Extraction of $\delta\langle r_c^2 \rangle$ for ${}^{6,7}\text{Li}$

We can now use the measured isotope shift between the stable isotopes to extract the change in the mean-square nuclear charge radius. This is an important test of our technique, because the result must be consistent with corresponding values extracted from other transitions or by other means, as long as those are model-independent. Therefore, we use the calculated mass shift  $\delta\nu_{\text{MS,Theory}}^{6,7}$  from Table III to extract by use of Eq. (62) the change in the ms nuclear charge radii and obtain

$$\delta\langle r^2 \rangle^{6,7} = -0.731(22) \text{ fm}^2. \quad (78)$$

Nuclear charge radii of the stable lithium isotopes were measured by elastic electron scattering in the 1960's and 70's [84–86] and results are summarized in [87, 88]. We used the charge radii  $R_c({}^7\text{Li}) = 2.39(3) \text{ fm}$  [84] and  $R_c({}^6\text{Li}) = 2.55(5) \text{ fm}$ , the average of the values reported in [85] and [86]. In Table XII the resulting value for  $\delta\langle r^2 \rangle^{6,7} = 0,79(29) \text{ fm}^2$  is compared with optical measurements of three transitions in lithium that have been repeatedly investigated during the last decades. Besides the  $2s \rightarrow 3s$  two-photon transition investigated here, isotope shifts were determined in the resonance lines

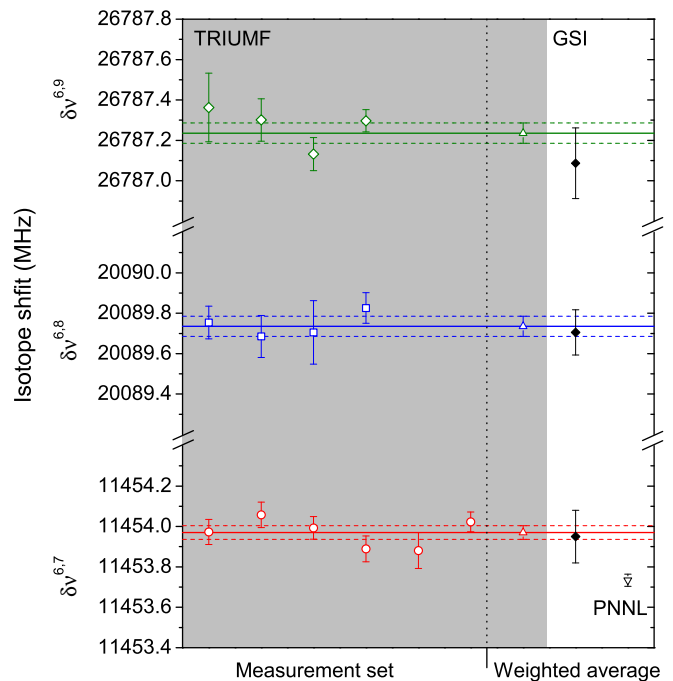


FIG. 18: Results of isotope shift measurements in the  $2s \rightarrow 3s$  transition for  ${}^7\text{Li}$ ,  ${}^8\text{Li}$  and  ${}^9\text{Li}$  at TRIUMF (left) as listed in Table XI. The average of all TRIUMF measurements ( $\Delta$ ) is plotted on the right and compared to the results of the GSI beamtime [1] for  ${}^{7,8,9}\text{Li}$  ( $\blacklozenge$ ) and a measurement of the stable isotopes ( $\nabla$ ) at the Pacific Northwest National Laboratory (PNNL) with a different technique [25]. Uncertainties include the statistical and the systematic uncertainty as listed in Table XI and discussed in the text.

$2s\ {}^2\text{S}_{1/2} \rightarrow 2p\ {}^2\text{P}_{1/2}$  ( $\text{D}_1$  line) and  $2s\ {}^2\text{S}_{1/2} \rightarrow 2p\ {}^2\text{P}_{3/2}$  ( $\text{D}_2$  line) in neutral lithium as well as in the  $1s2s\ {}^3\text{S}_1 \rightarrow 1s2p\ {}^3\text{P}_{0,1,2}$  transitions in  $\text{Li}^+$ . We use the recent mass shift calculations of Ref. [58] to extract  $\delta\langle r^2 \rangle^{6,7}$  from the isotope shifts in the  $\text{D}_1$  and  $\text{D}_2$  lines reported in the literature. The results are summarized in Table XII and also depicted in Fig. 19 in chronological order. The most reliable early result is obviously the measurement on  $\text{Li}^+$  by Riis *et al.* [14]. This experiment was performed using saturation spectroscopy on a fast ion beam in collinear and anticollinear geometry to obtain absolute transition frequencies in the  $1s2s\ {}^3\text{S}_1 \rightarrow 1s2p\ {}^3\text{P}_{0,1,2}$  transition for the two isotopes. The difference was then calculated to obtain the isotope shift. A crossed-beam experiment [89], where the laser crossed the ion beam under  $90^\circ$ , was in contradiction for the  $1s2p\ {}^3\text{P}_{1-2}$  fine structure splitting but the result by Riis *et al.* was confirmed in a later experiment using electrooptic modulation [90]. The change in charge radius between the stable isotopes extracted from the  $\text{Li}^+$  measurements [14] is in very good agreement with the elastic electron scattering result. In contrast, early measurements in the  $\text{D}_1$  and  $\text{D}_2$  line either disagree with the electron scattering value, for example [91], or the isotope shift in the two transitions and therefore the  $\delta\langle r^2 \rangle$  values obtained from them are in-

TABLE XI: Measured isotope shifts  $\delta\nu_{\text{IS}}^{6,A}$  in the  $2s^2S_{1/2} \rightarrow 3s^2S_{1/2}$  transition as obtained in all beamtimes at GSI and at TRIUMF and correction for the second-order Doppler-shift  $\delta\nu_{\text{SODS}}^{6,A}$ . All values are in kHz. A set of measurements includes typically 15 to 30 resonances at different Ti:Sa laser powers that were used to obtain one AC-Stark shift regression line as shown, for example, in Fig. 17. Results of sets are listed for the on-line beamtimes at TRIUMF. The uncertainty of each set is the  $1\sigma$  confidence limit of the AC-Stark extrapolation. If more than one set for an isotope was obtained during a beamtime, the average is listed in addition and printed in bold. The weighted average of all measurements for one isotope is marked “Average (ToPLiS)”. Here, the GSI measurement of  $^9\text{Li}$  was not included for reasons discussed in the text (Section IV D). The measured isotope shift has to be corrected for the differential second-order Doppler shift  $\delta\nu_{\text{SODS}}^{6,A}$  according to Eq. (77). The final corrected values are marked “Corrected (ToPLiS)”. Additional systematic uncertainties of 20 kHz +  $\Delta(\delta\nu_{\text{SODS}}^{6,A})$  (uncertainty of the second-order Doppler shift correction) must be considered for the isotope shift of  $^{7,8,9}\text{Li}$  and of  $\Delta_{\text{Syst}} = 85$  kHz as estimated for the isotope shift of  $^{11}\text{Li}$  and discussed in detail in Section IV D. The total uncertainty of the final corrected value is the geometrical sum of the statistical and the systematic uncertainty.

Facility Year	$\delta\nu^{6,7}$	$\delta\nu^{6,8}$	$\delta\nu^{6,9}$	$\delta\nu^{6,11}$
GSI 2003	11 453 950(130)	20 089 705(112)	26 787 087(175) <sup>a</sup>	-
TRIUMF 06/2004	11 453 973(62)			
TRIUMF 09/2004	<b>11 453 982(35)</b>		<b>26 787 217(61)</b>	
Set 1	11 454 058(63)	20 089 754(81)	26 787 363(170)	
Set 2	11 453 993(56)		26 787 301(105)	
Set 3	11 453 889(64)		26 787 132(82)	
TRIUMF 10/2004	<b>11 453 990(43)</b>	<b>20 089 767(57)</b>		
Set 1	11 453 881(89)	20 089 685(104)	26 787 297(55)	36 555 210(76)
Set 2	11 454 023(49)	20 089 705(157)		
Set 3		20 089 826(76)		
Average (ToPLiS)	11 453 981(24)	20 089 754(43)	26 787 261(41)	36 555 210(66)
$\delta\nu_{\text{SODS}}^{6,A}$	11(4)	19(6)	25(8)	34(11)
Corrected (ToPLiS)	11 453 970(34)	20 089 735(50)	26 787 236(50)	36 555 176(108)
PNNL [25]	11 453 734(30)			

<sup>a</sup> Not included in the total average for reasons discussed in Section IV D.

consistent, as is the case for the results reported in [92]. Similar, a recent measurement on an atomic beam using diode laser resonance fluorescence spectroscopy [93] reports isotope shifts in the  $D_1$  and  $D_2$  lines that are completely incompatible (not included in Fig. 19). The authors claim to have determined the absolute transition frequencies with accuracies of 30-60 kHz, which is much better than 1% of the observed linewidth, even though the hyperfine structure is not resolved and they had to fix the hyperfine structure spacings and the intensity ratios according to the Clebsch-Gordan coefficients in the fitting procedure. The extracted  $\delta\langle r^2 \rangle^{6,7}$  from the isotope shifts in the two transitions differ by more than 12 times the combined error bars. Hence, also the splitting isotope shift disagrees by about 1 MHz with theory. It is obvious that an accurate determination of the isotope shifts in the  $D_1$  and  $D_2$  lines of lithium is very difficult. The  $\text{Li}^+$  measurements [14] have the clear advantage that a Doppler-free technique was used which provides the required accuracy. Similarly, measurements in the  $2s \rightarrow 3s$  transition, as those reported here, are also to first-order Doppler-free and are not hampered by unresolved hyperfine splitting.

The first isotope shift measurement on the  $2s^2S_{1/2} \rightarrow$

$3s^2S_{1/2}$  transition reported by some of us in [25] seems to have some systematic offset, because it deviates in the  $D_1$  transition as well as in the two-photon transition from the now most accurate measurements. This was our only interferometric measurement on lithium and its deficiencies have been discussed above.

The experiments on the different transitions in lithium have been summarized and critically evaluated in [94]. Some recent measurements on the  $D_1$  and  $D_2$  lines resulted in a conclusive picture for  $\delta\langle r^2 \rangle^{6,7}$ : The optical results reported in [14, 95] and in this work (which includes [1, 2]) cover all discussed transitions and are consistent within their uncertainties. The weighted average of  $\delta\langle r^2 \rangle^{6,7}$  obtained from these optical investigations is  $0.740(15)$  fm<sup>2</sup> and agrees with the much less accurate result obtained by elastic electron scattering. Thus, we conclude that the atomic mass-shift calculations provide a consistent picture for all transitions investigated so far.

#### 4. Isotope shifts of $^{8,9}\text{Li}$

The isotope shifts of the isotopes  $^8\text{Li}$  and  $^9\text{Li}$  relative to  $^6\text{Li}$  were determined similar to the measurements of

TABLE XII: Changes in the mean-square nuclear charge radius  $\delta\langle r^2 \rangle^{6,7}$  between the stable isotopes  $^{6,7}\text{Li}$  from elastic electron scattering and optical isotope shifts in different transitions. Charge radii from optical isotope shifts were recalculated using the experimental value of the respective reference and the latest mass shift calculations (D<sub>1,2</sub> transitions from [58],  $2s \rightarrow 3s$  from this work). Different results for a given transition are therefore solely due to inconsistent isotope shift measurements. The weighted average of the bold printed values from [14, 95] and this work is  $0.740(15) \text{ fm}^2$  and is indicated in Fig. 19.

Experiment	$\delta\langle r^2 \rangle^{6,7} \text{ (fm}^2\text{)}$	Author	Ref.
electron scattering	-0.79(29)		[84–86]
Li $+ 1s2s\ ^3S_1 \rightarrow 1s2p\ ^3P_{0,1,2}$	<b>-0.735(36)</b>	Riis <i>et al.</i>	[14]
Li $2s\ ^2S_{1/2} \rightarrow 2p\ ^2P_{1/2}$	-0.32(24)	Sansonetti <i>et al.</i>	[91]
Li $2s\ ^2S_{1/2} \rightarrow 2p\ ^2P_{3/2}$	-0.41(20)	Sansonetti <i>et al.</i>	[91]
Li $2s\ ^2S_{1/2} \rightarrow 2p\ ^2P_{1/2}$	-0.415(61)	Scherf <i>et al.</i>	[92]
Li $2s\ ^2S_{1/2} \rightarrow 2p\ ^2P_{3/2}$	-0.975(61)	Scherf <i>et al.</i>	[92]
Li $2s\ ^2S_{1/2} \rightarrow 2p\ ^2P_{1/2}$	-0.875(53)	Walls <i>et al.</i>	[96]
Li $2s\ ^2S_{1/2} \rightarrow 3s\ ^2S_{1/2}$	-0.581(19)	Bushaw <i>et al.</i>	[25]
Li $2s\ ^2S_{1/2} \rightarrow 3s\ ^2S_{1/2}$	-0.719(83)	Ewald <i>et al.</i>	[1, 2] <sup>a</sup>
Li $2s\ ^2S_{1/2} \rightarrow 2p\ ^2P_{1/2}$	<b>-0.785(29)</b>	Noble <i>et al.</i>	[95]
Li $2s\ ^2S_{1/2} \rightarrow 2p\ ^2P_{3/2}$	<b>-0.687(42)</b>	Noble <i>et al.</i>	[95]
Li $2s\ ^2S_{1/2} \rightarrow 2p\ ^2P_{1/2}$	-0.857(16)	Das <i>et al.</i>	[93]
Li $2s\ ^2S_{1/2} \rightarrow 2p\ ^2P_{3/2}$	-0.344(28)	Das <i>et al.</i>	[93]
Li $2s\ ^2S_{1/2} \rightarrow 3s\ ^2S_{1/2}$	<b>-0.731(22)</b>	this work	

<sup>a</sup> Result included in the final value of this work.

the stable isotopes. A peculiarity of the radioactive isotope scans is the fact that ions implanted into the channeltron detector will inevitably decay there and produce  $\beta$ -delayed  $\alpha$  particles which will again trigger channeltron signals. This will on average result in more than one event per ionized atom and, thus, increase the detection efficiency. However, one has to ensure that the additional events are counted in the channel of that frequency applied to produce the photo ion. Otherwise, the line profile will be skewed depending on the scanning direction and the resonance center will be shifted. To avoid this effect, the radioactive ion beam was turned on only for 10 s for each frequency channel and turned off thereafter for at least five half-lives of the respective isotope (5 s for  $^8\text{Li}$ , 1 s for  $^{9,11}\text{Li}$ ). The events occurring during the beam-off time were still registered and added into the corresponding frequency channel. This was possible because the channeltron had a very small dark count rate on the order of 10 mHz and the applied detection technique of resonance ionization mass spectrometry is, apart from the dark count rate, practically background-free. We also looked for events from  $\beta$ -decay of the  $^{11}\text{Li}$  daughter  $^{11}\text{Be}$  ( $T_{1/2} = 13.8 \text{ s}$ ) and found nothing above background.”

The intensity of the radioactive ion beam was monitored with a NaI detector and a plastic scintillator mounted outside the vacuum chamber but close to the carbon catcher foil, detecting the  $\gamma$ -rays produced by  $\beta$  Bremsstrahlung in the stainless steel chamber and  $\beta$ -delayed neutrons.

Typical resonance profiles of  $^8\text{Li}$  and  $^9\text{Li}$  are shown in Fig. 20 (a,c). The count rate in each channel  $N_{\text{Raw}}$

was normalized to changing Ti:Sa laser powers and to variations in the ion beam intensity according to

$$N_{\text{Norm}} = N_{\text{Raw}} \cdot \left( \frac{N_\gamma}{\langle N_\gamma \rangle} \right)^{-1} \cdot \left( \frac{P_{\text{Ti:Sa}}}{\langle P_{\text{Ti:Sa}} \rangle} \right)^{-2}. \quad (79)$$

$N_\gamma$  is the  $\gamma$ -ray intensity observed with the plastic scintillator, and  $P_{\text{Ti:Sa}}$  is the Ti:Sa laser power recorded with the photodiode behind the resonator while recording the respective channel.  $\langle N_\gamma \rangle$  and  $\langle P_{\text{Ti:Sa}} \rangle$  are the average values during the complete scanning period. A correction for the  $\gamma$ -ray background was not necessary for  $^{8,9}\text{Li}$  since the count rate with the ion beam turned on was several orders of magnitude larger than the background with the ion beam turned off. The error bars of the data points in Fig. 20 include the statistical uncertainty as well as the propagated uncertainty from the normalization procedure.

Fitting was performed as for the stable isotopes and the center of gravity was calculated from the hyperfine component positions according to Eq. (66). As in the case of the stable isotopes, a small asymmetry in the line profile is observable in the residuals. It appears that the asymmetry is inverted for  $^9\text{Li}$  compared to the stable isotopes and  $^8\text{Li}$  as is the case for the order of the hyperfine components. Both is caused by the inverted frequency scale for the heavier isotope  $^9\text{Li}$ . The frequency of the Ti:Sa laser is measured relative to the iodine-locked diode laser ( $\nu_{\text{DL}}$ ). Resonance frequencies for  $^{6,7,8}\text{Li}$  are below the diode laser frequency while the  $^{9,11}\text{Li}$  resonances appear at higher frequencies.

Results of AC-Stark shift measurements for  $^{8,9}\text{Li}$  are

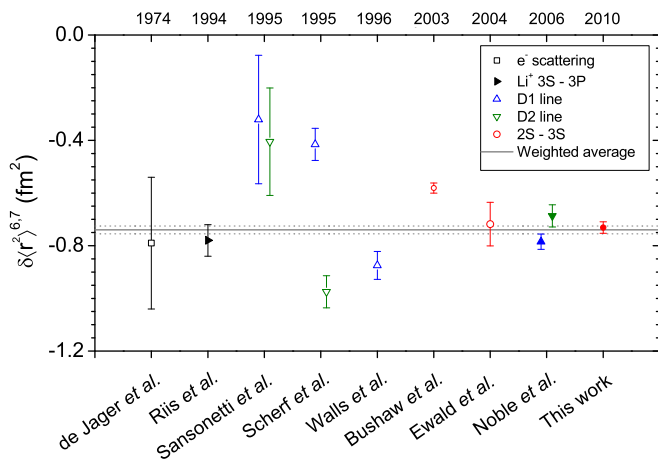


FIG. 19: Experimental results for the difference in the mean-square charge radius  $\delta \langle r^2 \rangle^{6,7}$  between the stable isotopes  ${}^6\text{Li}$  and  ${}^7\text{Li}$ . Besides the elastic electron scattering (square), all other experimental data are obtained from optical isotope shift measurements in different transitions in  $\text{Li}^+$  and neutral lithium as indicated in the figure legend and discussed in the text. Experimental results are depicted in chronological order. The weighted average of the latest data from the individual atomic lithium transitions (solid symbols) is indicated by the solid line with the respective uncertainty represented by the dashed lines. All values and respective references are listed in Table XII.

shown in Fig. 20 (b,d). The seemingly opposite slope of the lines is again due to the inverted frequency scale. As for the stable isotopes, the isotope shift is determined from the intercept of the regression line with the  $y$ -axis referenced to a similar measurement of the reference isotope  ${}^6\text{Li}$ . Measurements of  ${}^6\text{Li}$  were regularly interspersed between the ones on short-lived isotopes. The results for the isotope shift of  ${}^8\text{Li}$  and  ${}^9\text{Li}$  are included in Table XI. Four sets of measurements were obtained for each isotope during the two beamtimes at TRIUMF. The results of the different measurements and their averages are plotted in Fig. 18. Systematic uncertainties are similar as for the stable isotopes. The comparison with the measurements from GSI ( $\blacklozenge$ ) shows good agreement for both isotopes.

### 5. Isotope Shift of ${}^{11}\text{Li}$

The very short-lived isotope  ${}^{11}\text{Li}$  was available at TRIUMF with a yield of about 35 000 ions/s. A single scan of a  ${}^{11}\text{Li}$  resonance curve was acquired within approximately 10 min. Typically 5 to 7 consecutive individual scans were added to obtain a resonance signal as shown in Fig. 21. The small production rate of  ${}^{11}\text{Li}$  as compared with the other isotopes did not allow for full Ti:Sa laser power-series measurements since it was not possible to collect sufficient statistics at low laser power within a reasonable time. Thus, a different approach was used to correct for the AC-Stark shift of this isotope: All  ${}^{11}\text{Li}$

spectra were recorded at maximum laser power of the Ti:Sa laser and the average power value during the scan was evaluated. The count rate was normalized for ion beam and laser intensity fluctuations as described above for  ${}^8,9\text{Li}$ , but this time the background in the  $\gamma$  and neutron count rate of the plastic scintillator had to be taken into account. Therefore, the 1 s pause after each frequency step was used to determine the ion-beam independent background and to subtract it before normalization. The resonance signal was then fitted with the same line profile as applied to the other isotopes and the hyperfine center-of-gravity was determined. For reference, a complete AC-Stark shift power-series measurement of  ${}^6\text{Li}$  was performed at least once per day. Then, the AC-Stark shift function determined for  ${}^6\text{Li}$

$$\nu({}^6\text{Li}) = \nu_0({}^6\text{Li}) + b_1^{\text{Ti:Sa}} \cdot P_{\text{Ti:Sa}} \quad (80)$$

was evaluated at the average power  $\langle P_{\text{Ti:Sa}} \rangle_{11\text{Li}}$  during the  ${}^{11}\text{Li}$  measurements and the isotope shift was determined according to

$$\delta\nu^{6,11} = \nu({}^{11}\text{Li}) - (\nu_0({}^6\text{Li}) + b_1^{\text{Ti:Sa}} \cdot \langle P_{\text{Ti:Sa}} \rangle_{11\text{Li}}). \quad (81)$$

This procedure requires that the AC-Stark shift of both isotopes have the same slope  $b_1^{\text{Ti:Sa}}$ . This is theoretically expected since all resonance frequencies in the  $2s \rightarrow 3s$  transition are far-off from any allowed E1 transition that would connect the  $2s$  or  $3s$  level to a  $p$  state. In fact, this was also experimentally verified for all other lithium isotopes as will be described in the next Section.

In total, 24 resonances could be measured for  ${}^{11}\text{Li}$ . The distribution of the extracted isotope shift values  $\delta\nu^{6,11}$  is shown in Fig. 22 (open circles). The weighted average is included in Table XI. The uncertainty was estimated as the standard error of the mean as depicted in the figure. This is in accordance with the uncertainties obtained for the more abundant isotopes discussed above.

### D. Systematic uncertainties in the isotope shift

Several effects that can possibly affect the extracted resonance position were investigated. These include deviations from the Lorentzian, respectively Voigtian resonance lineshape, isotope-dependent slopes or nonlinearities in the AC-Stark shift correction, and the influence of stray magnetic fields.

It was found that the most crucial effect is an isotope-dependent slope of the regression line in the AC-Stark correction. This does not matter for the stable and the less exotic isotopes  ${}^6\text{--}9\text{Li}$  since those were all measured at different powers and extrapolated to zero laser intensity. However, the slope for  ${}^{11}\text{Li}$  could not be measured experimentally and a difference in the slope between  ${}^{11}\text{Li}$  and the reference isotope  ${}^6\text{Li}$  would directly influence the extracted isotope shift. Therefore, the slopes from all  ${}^6\text{--}9\text{Li}$  AC-Stark shift measurements at TRIUMF were compared after the first on-line beamtime. Previous measurements at GSI showed no indication for an

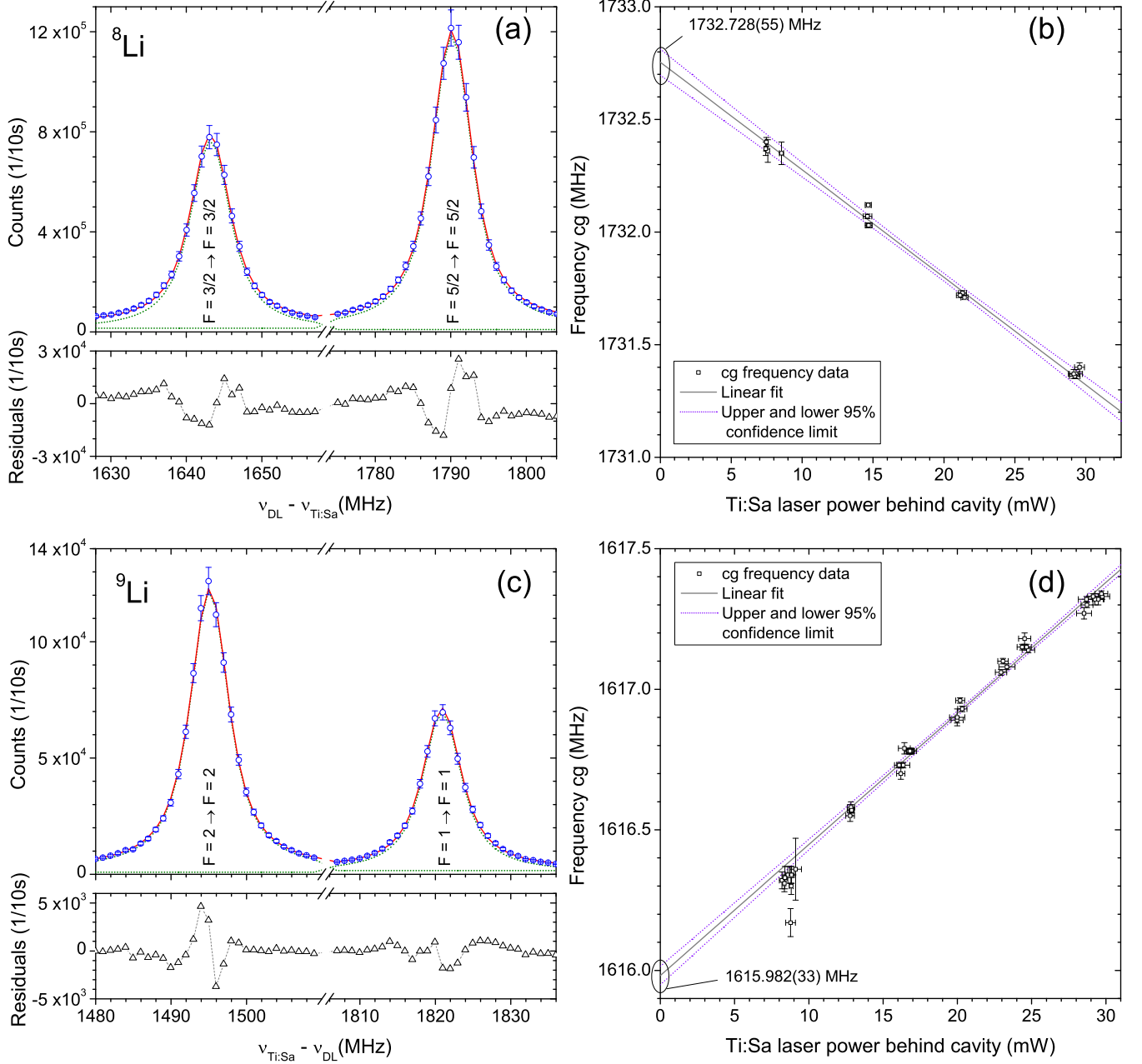


FIG. 20: Typical spectra (a,c) and AC-Stark shift results (b,d) for  $^8\text{Li}$  and  $^9\text{Li}$ . Data points of the spectra are normalized to intensity variations of the ion beam and laser beam according to Eq. (79). Voigt profiles with Doppler pedestal are fitted to the hyperfine resonances with the same procedure as used for the stable isotopes. The solid lines in (a) and (c) are the common fit results while the dashed lines are the line profiles of the individuals components. Results of AC-Stark shift measurements are plotted in (b) and (d) for  $^8\text{Li}$  and  $^9\text{Li}$ , respectively. The solid line is the result of a linear regression and the dashed lines indicate the 95% confidence band. The intercept of the regression lines with the  $y$ -axis is used to determine the isotope shift.

isotope-dependent slope in the AC-Stark shift of  $^{6,7,8}\text{Li}$  within the level of accuracy of approximately 2 kHz/mW. However, at TRIUMF the AC-Stark shift showed larger isotope-dependent trends. This can be seen in the left part of Fig. 23 where this is indicated by the straight lines. There is a clear offset between  $^7\text{Li}$  and  $^8\text{Li}$ , and the reference isotope  $^6\text{Li}$  shows even a small drift. This effect was found to be an artefact caused by interference

effects in the viewport behind the optical resonator. The geometry of the vacuum chamber, the resonator and the viewport is depicted in Fig. 10. While the entrance window was antireflection coated, the exit window behind the resonator was uncoated. The plane-parallel surfaces of the 5 mm thick window gave rise to an etalon effect, and thus the amount of light detected on the photodiodes was wavelength-dependent and therefore different

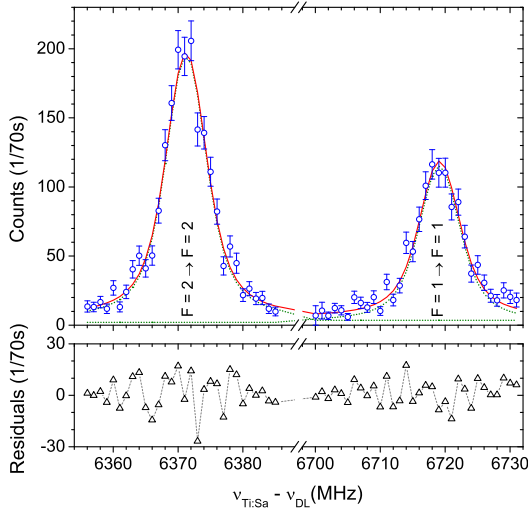


FIG. 21: Typical spectrum of  $^{11}\text{Li}$  as it was obtained in the beamtime at TRIUMF. Data points are normalized to intensity fluctuations of the ion and laser beams. The solid line is again the common fit function of the two hyperfine components while the dotted lines are the contributions of the individual hyperfine components.

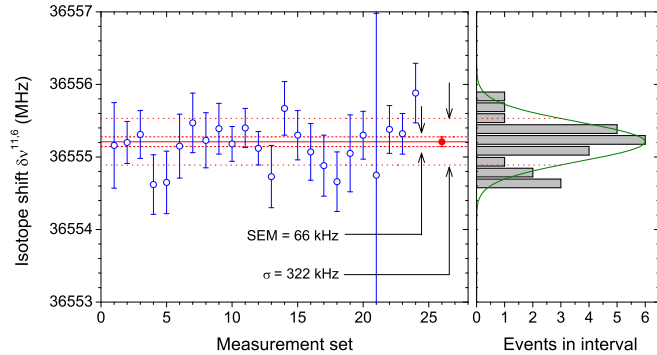


FIG. 22: Distribution and the average of the  $^{11}\text{Li}$  -  $^6\text{Li}$  isotope shift (center of gravity) of all 24  $^{11}\text{Li}$  resonances obtained at TRIUMF. The dotted lines represent the standard deviation ( $\sigma$ ) of the individual measurements and the dashed ones the standard error of the mean. The average value is plotted as solid circle. A histogram of the measured frequencies is depicted on the right.

from isotope to isotope since the free-spectral-range of the window-etalon was comparable to the isotope shift between  $^6\text{Li}$  and  $^{11}\text{Li}$ . A direct measurement of this effect was performed by comparing the amount of light entering the vacuum chamber and leaving it. The etalon effect was clearly observed and the plane-parallel window was replaced by a wedged window. A second measurement after the replacement did not show a detectable wavelength-dependent variation anymore.

AC-Stark shift coefficients that were measured after the replacement are plotted in the right part of Fig. 23. There is still a slow drift of the coefficients with time, which might be caused by a slow degradation of the mir-

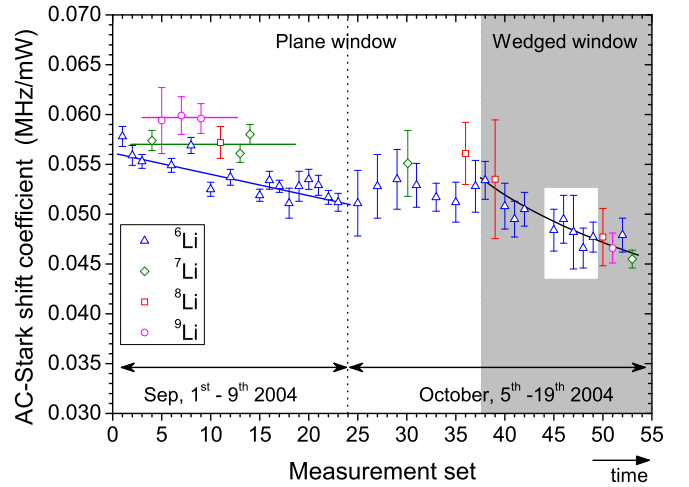


FIG. 23: Experimentally determined AC-Stark shift coefficients  $b_1^{\text{Ti:Sa}}$  for all measurement sets and all isotopes conducted at TRIUMF. The periods of the two beamtimes are indicated at the bottom. Measurements 1-37 were performed with a plane parallel viewport window while later measurements (gray background) were carried out with a wedged window to avoid interference effects. The lines are included to guide the eye along the measurements of the respective isotope (left) and to indicate the common drift after the replacement of the viewport with a wedged window. The highlighted part on the right indicates the period in which all  $^{11}\text{Li}$  resonances were recorded.

ror reflectivity, but all isotopes show equal coefficients within the uncertainty. To estimate the remaining systematic uncertainty for the  $^{11}\text{Li}$  measurements, the standard deviation of the slope coefficients for the reference isotope within the periode of  $^{11}\text{Li}$  measurements, as indicated in the figure, was determined ( $\sigma = 0.81 \text{ kHz/mW}$ ) and multiplied with the average Ti:Sa laser power on the photodiode during all measurements (30 mW). Since much less measurements were performed for  $^{11}\text{Li}$  than for the other isotopes, the AC-Stark shift of the dye laser might not be fully included in the statistical uncertainty. Therefore, a systematic contribution was estimated by multiplying the slope of the AC-Stark shift caused by the dye laser (Eq. (71), obtained from Fig. 15) with the standard deviation of the dye laser power as measured on the photodiode during all  $^{11}\text{Li}$  measurements. This resulted in systematic uncertainties of 46 kHz for the shift induced by the intensity of the Ti:Sa laser light and of 8 kHz by that of the dye laser. These values are listed in Table XIII.

The observation of this interference effect is the reason why the  $^9\text{Li}$  isotope shift measurement at GSI was excluded in the final average: Insufficient statistics did not allow us to perform an AC-Stark shift measurement for this isotope at GSI. Instead, a measurement as for  $^{11}\text{Li}$  at TRIUMF was carried out but with the plane-parallel viewport. Therefore the value might be systematically shifted. However, the reasonable agreement with

the TRIUMF data within the uncertainty shows that the size of a possible systematic contribution was reasonably estimated in [1].

Recoil effects are not important for two-photon transitions, since the momenta of the two photons cancel and the velocity of the atom stays constant during the excitation process. The differential second-order Doppler shift correction  $\delta\nu_{\text{SOD}}^{6,A}$  was already discussed and its uncertainty is included in the systematic uncertainty.

The influence of unresolved Zeeman splitting in the hyperfine structure has been theoretically estimated by calculating the effect of the 0.7 G stray magnetic field measured at the beamline. A large part of the induced shifts in the  $2s$  and  $3s$  levels cancels. The remaining part shifts the peak positions of the two hyperfine components by only about 10 kHz in opposite directions. Thus, the center-of-gravity of the hyperfine structure is expected to stay constant. For safety, the total expected shift of  $\approx 10$  kHz is included in the error budget for the isotope shift (Table XI) as well as for the hyperfine splitting (Table X).

Finally, the small asymmetry in the peak profile has to be considered. This was observed much more pronounced in off-line measurements at GSI which were carried out very recently in order to determine the absolute frequency of the  $2s \rightarrow 3s$  transition. The asymmetry was attributed to the position-dependent AC-Stark shift that the atoms experience when they cross the Gaussian laser beam profile [27]. The strongest shift occurs in the beam center but all atoms that are excited and ionized in the wings of the laser beam are less AC-Stark shifted and are therefore causing an asymmetry of the lineshape. This assumption was supported by lineshape simulations which are presented in detail in [27]. There it was shown that the asymmetry leads to a small shift in the position and results in a small deviation of the AC-Stark shift behavior from a straight line at very low power. This is crucial concerning the absolute transition frequency, but the isotope dependence was found to be very small ( $\lesssim 10$  kHz). This value was added to the systematic uncertainty for all isotopes.

All effects contributing to the uncertainty of the  $^{11}\text{Li}$  -  $^6\text{Li}$  isotope shift are summarized in Table XIII. Even though the systematic uncertainties are mutually independent and will not necessarily cause a shift in the same direction, we have added them linearly to obtain the total systematic uncertainty which is then geometrically added to the statistical uncertainty. In total, a relative uncertainty of the  $^{6,11}\text{Li}$  isotope shift of  $3 \cdot 10^{-6}$  was obtained in this work.

For the other isotopes, power fluctuations of the dye laser are included in the statistical uncertainty given in Table XI. The Zeeman splitting (10 kHz), the lineshape asymmetry (10 kHz) and the uncertainty in the second-order Doppler shift are correlated for all isotopes and have therefore been linearly added to the total systematic uncertainty. The geometric sum of the systematic and the uncorrelated statistical contribution is then taken as the final isotope shift as listed in Table XI.

## V. CHANGES IN THE MEAN-SQUARE CHARGE RADIUS

The measured isotope shifts (Table XI) can now be combined with the mass shift calculations discussed in Section II F (Table III) to extract by use of Eq. (62) the change in the rms nuclear charge radii  $\delta\langle r^2 \rangle$  along the lithium chain of isotopes. Results are listed in Table XIV and plotted in Fig. 24 relative to  $^6\text{Li}$ . This table repre-

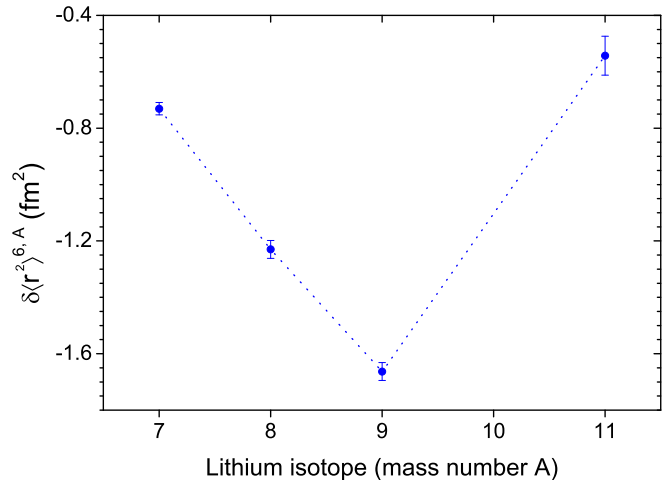


FIG. 24: Changes  $\delta\langle r^2 \rangle^{6,A}$  in the mean-square charge radius along the lithium isotope chain with respect to the mean-square nuclear charge radius of  $^6\text{Li}$ . The values are obtained from the measured isotope shift (Table XI) and theoretical mass shift calculations (Table III) using Eq. (62).

sents the summary of the complete analysis of the experimental results and theoretical mass shift calculations. We want to stress that slightly varying mass shift values along previous publications on this topic [3, 29, 57, 58] are not caused by a model-dependence of the mass shift calculations but several improvements: First, since the start of the experiments the accuracy of the atomic calculations could be improved by an order of magnitude; second, more accurate atomic masses became available by mass measurements at MISTRAL [97, 98] and TITAN [53]; third, the influence of the nuclear polarizability on the transition frequency could be calculated for the first time [29]. Hence, previous values should not be used anymore for calculating the nuclear charge radii.

Figure 24 clearly depicts the trend in the nuclear charge radii: The size of the proton distribution shrinks continuously from  $^6\text{Li}$  to  $^9\text{Li}$ . As already stated in [3] this reduction is attributed to the strong clusterization of the lithium nuclei. Clusterization is a phenomenon that often appears in light nuclei; they tend to behave as composed of well-defined subsystems, called “clusters.” Experimentally, this is reflected in the fact that  $\alpha$ -particles, tritons ( $t = ^3\text{H}$ ), and helions ( $^3\text{He}$ ) can be knocked out from a number of nuclei with substantial probability. Often  $\alpha$  clusterization is observed even in heavier stable nuclei along the  $N = Z$  line, for example in  $^{12}\text{C}$  or  $^{16}\text{O}$ .

TABLE XIII: Summary of statistical and systematic uncertainties of the corrected  $^{11}\text{Li} - ^6\text{Li}$  isotope shift  $\delta\nu_{\text{IS}}^{6,11}$ . Systematic uncertainties arise from slope variations in the AC-Stark shift induced by the Ti:Sa or dye laser induced between  $^{11}\text{Li}$  and  $^6\text{Li}$ , unresolved Zeeman splitting caused by the stray magnetic fields (0.7 G), a lineshape asymmetry caused by a position-dependent AC-Stark shift in the laser beam intensity profile as discussed in detail in [27], and from second-order Doppler shift. All systematic contributions are linearly added. The total uncertainty is the geometrical sum of the statistical and the systematic contributions.

Effect	Contribution
Statistical uncertainty (standard error of the mean for 24 measurements)	66 kHz
AC-Stark shift induced by the Ti:Sa laser	46 kHz
AC-Stark shift induced by the dye laser	8 kHz
Unresolved Zeeman splitting	10 kHz
Lineshape asymmetry	10 kHz
Second-order Doppler shift	11 kHz
Total	109 kHz

According to nuclear structure calculations,  $^6\text{Li}$  can be described as  $\alpha + d$ ,  $^7\text{Li}$  as  $\alpha + t$ , and the heavier isotopes as  $\alpha + t + xn$  with  $x = 1, 2$  for  $^8, 9\text{Li}$ , respectively. The consequence of clusterization is a strong center-of-mass (cm) motion of the clusters that leads to larger proton distributions. This cm motion is obviously reduced with increasing number of neutrons, hence, the nuclear charge radius decreases. This trend is reversed when going from  $^9\text{Li}$  to  $^{11}\text{Li}$ . Here the charge radius increases again and  $^{11}\text{Li}$  is similar in size to  $^7\text{Li}$ . There are in general two effects that can be made responsible for this increase: Either the  $^9\text{Li}$  core of  $^{11}\text{Li}$  is changed in its internal structure, *i.e.* core polarization takes place, or the correlation of the halo neutrons induces a cm motion of the  $^9\text{Li}$  core nucleus.

Core polarization is related to the neutron- $^9\text{Li}$  interaction and the internal structure of  $^9\text{Li}$ , whereas the center-of-mass motion gives insight into the neutron-neutron correlation in the three-body system. Pure three-body calculations assume the core to be inert (“frozen core” approximation) whereas more elaborated nuclear models try to take both effects into account. There is experimental evidence that the frozen core assumption is a very good approximation, however, both effects might contribute to the total change in the charge radius between  $^9, 11\text{Li}$  and it is impossible to disentangle their contributions without consideration of further experimental data or theory. More complete theoretical models were considered in [1, 3] and will be discussed in more detail in a following publication [28].

Comparison with nuclear models can best be performed if absolute charge radii are calculated from the measured isotope shift. However, we need the charge radius of one reference isotope to fix the absolute charge radius. The value for the charge radius obtained by this procedure is model-dependent if the reference radius is obtained using a nuclear model. This is the case for the charge radii from elastic electron scattering of lithium, because the model-independent approach gave rather large uncertainties [86]. Since the value of  $\delta\langle r^2 \rangle^{6,7}$  ob-

TABLE XIV: Field shifts contributions  $\delta\nu_{\text{FS}}^{6,A}$  in the  $2s \rightarrow 3s$  transition of the lithium isotopes (extracted from the measured isotope shifts in Table XI by subtracting the theoretically evaluated mass shift contributions listed in Table III), field shift coefficients  $C$  as defined by Eq. (60), and the change in the mean-square nuclear charge radius  $\delta\langle r^2 \rangle^{6,A}$  between the isotope  $^A\text{Li}$  and the reference isotope  $^6\text{Li}$  calculated using Eq. (62).

$^A\text{Li}$	Field Shift (MHz)	$C$ (MHz/fm $^2$ )	$\delta\langle r^2 \rangle^{6,A}$ (fm $^2$ )
$^7\text{Li}$	1.149(34)	-1.5719(16)	-0.731(22)
$^8\text{Li}$	1.933(51)	-1.5719(16)	-1.230(32)
$^9\text{Li}$	2.615(50)	-1.5720(16)	-1.663(32)
$^{11}\text{Li}$	0.852(108)	-1.5703(16)	-0.543(69)

tained in our isotope shift measurement is slightly different from that obtained by elastic electron scattering [87] (even though within uncertainties), the absolute charge radii differ if they are based either on the charge radius reported for  $^6\text{Li}$  [85, 86] or that reported for  $^7\text{Li}$  [84]. In previous publications, we have used  $r_c(^7\text{Li}) = 2.39(3)$  fm from [84] which is not model-independent and a recent analysis of the world scattering data revealed that the charge radius of  $^6\text{Li}$  is better understood. Since this topic is of major importance for the comparison with nuclear structure models and for conclusions about the structure of the halo nucleus, it is discussed in more detail in the following publication [28].

## VI. SUMMARY

This long writeup reports about the isotope shift measurement of the complete lithium isotope chain from the stable isotopes up to the exotic two-neutron halo nucleus  $^{11}\text{Li}$ . The theory of atomic mass shift calculations is explained in detail and the most accurate results for the mass shifts in the  $2s\ ^2S_{1/2} \rightarrow 3s\ ^2S_{1/2}$  two-



photon transition are presented. The experimental setup for high-accuracy resonance ionization mass spectroscopy with cw lasers, including a two-photon transition is described with all important details to judge the quality and accuracy of the data obtained. All sources of possible systematic uncertainties in these measurements that are known to us are evaluated and discussed. Compared to previous publications, a small additional correction for the second-order Doppler shift is included in the isotope shift result. Combination of the accurate measurements with the mass shift calculations allows us to extract the changes in the nuclear charge radii along the isotope chain spanning from the stable  ${}^6\text{Li}$  to the halo nucleus  ${}^{11}\text{Li}$ . Absolute nuclear charge radii will be extracted and compared with predictions by nuclear models in a following publication.

### Acknowledgments

This work is supported by BMBF (contract No. 06TU203, 06TU263I, 06MZ215) and by the Helmholtz

Association of German Research Centres (contract VH-NG 148). Support from the U. S. DOE Office of Science (B. A. B. ), NRC through TRIUMF, NSERC and SHARCnet (G. W. F. D. and Z.-C. Y.) is acknowledged. A. W. was supported by a Marie-Curie Fellowship of the European Community Programme IHP under contract number HPMT-CT-2000-00197. K. P. and M. P. acknowledge support by the NIST Precision Measurement Grants. We thank the target laboratory at GSI for providing the carbon foil catcher, Nikolaus Kurz, Mohammad Al-Turany, Christophor Kozhuharov (GSI) and the ISAC Computer Division at TRIUMF for support in data acquisition, Reinhard Kirchner, Haiming Wang, Frank Schmitt and Sascha Faber for contributions during the early part of this experiment, Melvin Good for help during installation of the experiment at TRIUMF, and René Roy for providing a liquid scintillator. The role of Isao Tanihata for motivating and initiating these experiments is particularly acknowledged by the authors.

- 
- [1] G. Ewald *et al.*, Phys. Rev. Lett. **93** 113002 (2004).
  - [2] G. Ewald *et al.*, Phys. Rev. Lett. **94** 039901 (2005).
  - [3] R. Sánchez *et al.*, Phys. Rev. Lett. **96** 033002 (2006).
  - [4] W. E. Otten: *Nuclear Radii and Moments of Unstable Isotopes*, Treatise of Heavy-Ion Physics, Vol. 8, Plenum Press, New York (1987).
  - [5] J. Billowes and P. Campbell, J. Phys. G, **21**, 707 (1995).
  - [6] R. Neugart, Europ. Phys. J. A, **15**, 35 (2002).
  - [7] H.-J. Kluge and W. Nörtershäuser, Spectrochim. Acta B, **58**, 1031 (2003).
  - [8] W. Geithner *et al.*, Hyperfine Interact. **127**, 117 (2000).
  - [9] W. Geithner *et al.*, Phys. Rev. C **71**, 064319 (2005).
  - [10] G. W. F. Drake, in *Long-range Casimir forces: Theory and recent experiments on atomic systems*, edited by F.S. Levin and D.A. Micha (Plenum, New York, 1993), pp. 107–217.
  - [11] F. Schmidt-Kaler, D. Leibfried, S. Seel, C. Zimmermann, W. König, M. Weitz, and T. W. Hänsch, Phys. Rev. Lett. **51** 2789 (1995).
  - [12] A. Huber, T. Udem, B. Gross, J. Reichert, M. Kourogi, K. Pachucki, M. Weitz, and T. W. Hänsch, Phys. Rev. Lett. **80** 468 (1998).
  - [13] D. Shiner, R. Dixson, and V. Vedantham, Phys. Rev. Lett. **74** 3553 (1995).
  - [14] E. Riis, A. G. Sinclair, O. Poulsen, G. W. F. Drake, W. R. C. Rowley, and A. P. Levick, Phys. Rev. A, **49**, 207 (1994).
  - [15] H. Backe, A. Dretzke, M. Hies, G. Kube, H. Kunz, W. Lauth, M. Sewtz, N. Trautmann, R. Repnow, and H. J. Maier, Hyperfine Interact. **127** 35 (2000).
  - [16] L.-B. Wang *et al.*, Phys. Rev. Lett. **93** 142501 (2004).
  - [17] T. Nakamura, *et al.*, Phys. Rev. Lett. **96**, 252502, (2006).
  - [18] E. Arnold, J. Bonn, R. Gegenwart, W. Neu, R. Neugart, E. W. Otten, G. Ulm, K. Wendt and The Isolde Collaboration, Phys. Lett. B **197** 311 (1987).
  - [19] E. Arnold *et al.*, Phys. Lett. B **281** 16 (1992).
  - [20] E. Arnold, J. Bonn, A. Klein, P. Lievens, R. Neugart, M. Neuroth, E. W. Otten, H. Reich, and W. Widdra, Z. f. Phys. A **349** 337 (1994).
  - [21] D. Borremans *et al.*, Phys. Rev. C **72** 044309 (2005).
  - [22] R. Neugart *et al.*, Phys. Rev. Lett. **101** 132502 (2008).
  - [23] W. Nörtershäuser *et al.*, Phys. Rev. Lett. **102** 062503 (2009).
  - [24] M. Žáková *et al.*, J. Phys. G: Nucl. Part. Phys. **37** 055107 (2010).
  - [25] B. A. Bushaw, W. Nörtershäuser, G. Ewald, A. Dax, and G. W. F. Drake, Phys. Rev. Lett. **91** 043004 (2003).
  - [26] T. Udem, A. Huber, B. Gross, J. Reichert, M. Prevedelli, M. Weitz, and T. W. Hänsch, Phys. Rev. Lett. **79**, 2646 (1997).
  - [27] R. Sánchez *et al.*, New J. Phys. **11** 073016 (2009).
  - [28] W. Nörtershäuser *et al.*, in preparation (2010).
  - [29] M. Puchalski, A. M. Moro, and K. Pachucki, Phys. Rev. Lett. **97**, 133001 (2006).
  - [30] M. Puchalski and K. Pachucki, Hyperfine Interact. **196** 35 (2010).
  - [31] G. W. F. Drake and Z.-C. Yan, Phys. Rev. A, **46**, 2378 (1992).
  - [32] G. W. F. Drake: Adv. At. Mol. Opt. Phys. **31**, 1 (1993).
  - [33] Z.-C. Yan and G. W. F. Drake, Phys. Rev. Lett. **81**, 774 (1998).
  - [34] Z.-C. Yan and G. W. F. Drake, Phys. Rev. A, **66**, 042504 (2002).
  - [35] Z.-C. Yan and G. W. F. Drake, Phys. Rev. Lett., **91**, 113004 (2003).
  - [36] M. Puchalski and K. Pachucki, Phys. Rev. A **73**, 022503 (2006).
  - [37] Z.-C. Yan and G. W. F. Drake, Phys. Rev. A **52**, 3711 (1995).
  - [38] Z.-C. Yan, M. Tambasco, and G. W. F. Drake, Phys.

- Rev. A **57**, 1652 (1998).
- [39] A. P. Stone, Proc. Phys. Soc. **77**, 786 (1961); **81**, 868 (1963).
- [40] L. I. Schiff, *Quantum Mechanics* (3rd edition, McGraw-Hill Book Company, 1968).
- [41] P. K. Kabir and E. E. Salpeter, Phys. Rev. **108**, 1256 (1957).
- [42] H. Araki, Prog. Theor. Phys. **17**, 619 (1957).
- [43] J. Sucher, Phys. Rev. **109**, 1010 (1958).
- [44] M. I. Eides, H. Grotch, and V.A. Shelyuto, Phys. Rep. **342**, 63 (2001).
- [45] K. Pachucki, J. Phys. B **31**, 5123 (1998).
- [46] K. Pachucki and J. Sapirstein, J. Phys. B **33**, 455 (2000).
- [47] G. W. F. Drake and W. C. Martin, Can. J. Phys. **76**, 679 (1998).
- [48] G. W. F. Drake and S. P. Goldman, Can. J. Phys. **77**, 835 (1999).
- [49] W. Leidemann and R. Rosenfelder, Phys. Rev. C **51**, 427 (1995).
- [50] J. L. Friar and G. L. Payne, Phys. Rev. C **56**, 619 (1997).
- [51] K. Pachucki, D. Leibfried, and T. W. Hänsch, Phys. Rev. A **48**, R1 (1993);
- [52] K. Pachucki, M. Weitz, and T. W. Hänsch, Phys. Rev. A **49**, 2255 (1994).
- [53] M. Smith *et al.*, Phys. Rev. Lett. **101**, 202501 (2008).
- [54] J. L. Friar, Phys. Rev. C **16**, 1540 (1977).
- [55] G. Audi, A. H. Wapstra, and C. Thibault, Nucl. Phys. A **729** 337 (2003).
- [56] S. Nagy, T. Fritioff, M. Suhonen, R. Schuch, K. Blaum, M. Björkhage, and I. Bergström, Phys. Rev. Lett. **96**, 163004 (2006).
- [57] M. Puchalski and K. Pachucki, Phys. Rev. A **78** 052511 (2008).
- [58] Z.-C. Yan, W. Nörtershäuser, and G. W. F. Drake, Phys. Rev. Lett. **100** 243002 (2008).
- [59] K. Pachucki and J. Sapirstein, J. Phys. B At. Mol. Opt. Phys. **36**, 803 (2003).
- [60] J. L. Friar, Ann. Phys. (N.Y.) **122**, 151 (1979).
- [61] M. Dombisky, D. Bishop, P. Bricault, D. Dale, A. Hurst, K. Jayamanna, R. Keitel, M. Olivo, P. Schmor, and G. Stanford, Rev. Sci. Instrum. **71**, 978 (2000).
- [62] J. F. Ziegler, SRIM - the stopping range of ions in matter. <http://www.srim.org/>, 2003.
- [63] F. Schmitt, A. Dax, R. Kirchner, H.-J. Kluge, T. Kühl, I. Tanihata, M. Wakasugi, H. Wang, and C. Zimmermann, Hyperfine Interact. **127**, 111 (2000).
- [64] B. A. Bushaw, Progress in Analytical Spectroscopy **12**, 247 (1989).
- [65] K. Blaum, C. Geppert, P. Müller, W. Nörtershäuser, K. Wendt, and B. A. Bushaw, Int. J. Mass. Spectrom. **202** 81 (2000).
- [66] K. Blaum, C. Geppert, P. Müller, W. Nörtershäuser, E. W. Otten, A. Schmitt, N. Trautmann, K. Wendt, and B. A. Bushaw, Int. J. Mass. Spectrom. **181** 67 (1998).
- [67] K. Wendt *et al.*, Fresenius J. Anal. Chem. **364** 471 (1999).
- [68] B. A. Bushaw and W. Nörtershäuser, Eur. Phys. J. D **55** 1679 (2000).
- [69] H. Knöckel, B. Bodermann, and E. Tiemann, *Iodine Spectrum Calculating Software Iodine Spec 4*, Toptica Photonics (2004).
- [70] S. Reinhardt, B. Bernhardt, C. Geppert, R. Holzwarth, G. Huber, S. Karpuk, N. Miski-Oglu, W. Nörtershäuser, C. Novotny, and T. Udem, Opt. Commun. **274**, 354 (2007).
- [71] J.L. Hall, L. Hollberg, T. Baer, and H. G. Robinson, Appl. Phys. Lett. **39**, 681 (1981).
- [72] N. C. Wong and J. L. Hall, J. Opt. Soc. Am. B **2** 1527 (1985).
- [73] P. Russel, Science **299**, 358 (2003).
- [74] R. W. P. Drever, J. L. Hall, F. V. Kowalski, J. Hough, G. M. Ford, A. J. Munley, and H. Ward, Appl. Phys. B **31**, 97 (1983).
- [75] E.D. Black, Am. J. Phys. **69**, 79 (2001).
- [76] W. H. Press, S. A. Teukolsky, W. T. Vetterling, and B. P. Flannery, *Numerical Recipes in C* (Cambridge University Press, Cambridge, 1996).
- [77] G. Grynberg and B. Cagnac, Rep. Prog. Phys **40** 791 (1977).
- [78] L. J. Radziemski, J. R. Engleman, and J. W. Brault, Phys. Rev. A **52**, 4462 (1995).
- [79] E. Arimondo, M. Inguscio, and P. Violino, Rev. Mod. Phys. **49** 31 (1977).
- [80] G. D. Stevens, C.-H. Iu, S. Williams, T. Bergemann, and H. Metcalf, Phys. Rev. A. **51**, 2866 (1995).
- [81] Z.-C. Yan, D. K. McKenzie, and G. W. F. Drake, Phys. Rev. A **54** 1322 (1996).
- [82] M. Godefroid, C. F. Fischer, and P. Jönsson, J. Phys. B: At. Mol. Opt. Phys. **34** 1079 (2001).
- [83] A. Beckmann, K. D. Böklen, and D. Elke, Z. f. Phys. **270** 173 (1974).
- [84] L. R. Suelzle, M. R. Yearian, and H. Crannell, Phys. Rev. **132** 992 (1967).
- [85] C. C. Li, I. Sick, R.R. Whitney, and M.R. Yearian, Nucl. Phys. A **162** 583 (1971).
- [86] F. A. Bumiller, F. R. Buskirk, J. N. Dyer, and W. A. Monson, Phys. Rev. C **5** 391 (1972).
- [87] C. W. de Jager, H. deVries, and C. deVries, At. Data Nucl. Data Tables **14**, 479 (1974).
- [88] H. deVries, C.W. de Jager, and C. Devries, At. Data Nucl. Data Tables **36** 495 (1987).
- [89] H. Rong, S. Grafström, J. Kowalski, G. zu Putlitz, W. Jastrzebski and R. Neumann, Z. Phys. D: At. Mol. Clusters **25**, 337 (1993).
- [90] W. A. van Wijngaarden, Adv. At. Mol. Opt. Phys. **36**, 141 (1996).
- [91] C. J. Sansonetti, B. Richou, R. Engleman Jr., and L. J. Radziemski, Phys. Rev. A **52**, 2682 (1995).
- [92] W. Scherf, O. Khait, H. Jäger and L. Windholz, Z. f. Phys. D **36**, 31 (1996).
- [93] D. Das and V. Natarajan, Phys. Rev. A **75**, 052508 (2007).
- [94] G. A. Noble and W. A. Van Wijngaarden, Can. J. Phys. **87** 807 (2009).
- [95] G. A. Noble, B. E. Schultz, H. Ming, and W. A. Van Wijngaarden, Phys. Rev. A **74** 012502 (2006).
- [96] J. Walls, R. Ashby, J. J. Clarke, B. Lu and W. A. v. Wijngaarden, Eur. Phys. J. D **22**, 159 (2003).
- [97] C. Bachelet, G. Audi, C. Gaulard, C. Guénaut, F. Herfurth, D. Lunney, M. De Saint Simon C. Thibault, and the ISOLDE Collaboration, Eur. Phys. J. A **25**, 31 (2005).
- [98] C. Bachelet, G. Audi, C. Gaulard, C. Guenaut, F. Herfurth, D. Lunney, M. De Simon, and C. Thibault, Phys. Rev. Lett. **100**, 182501 (2008).